J. Fluid Mech. (2013), *vol.* 734, *pp.* 456–485. © Cambridge University Press 2013
doi:10.1017/jfm.2013.483

Consequences of viscous anisotropy in a deforming, two-phase aggregate. Part 2. Numerical solutions of the full equations

Richard F. Katz[1,†] **and Yasuko Takei**[2]

[1]Department of Earth Sciences, University of Oxford, Oxford OX1 3AN, UK
[2]Earthquake Research Institute, University of Tokyo, Tokyo 113-0032, Japan

(Received 5 November 2012; revised 14 June 2013; accepted 11 September 2013)

In partially molten regions of Earth, rock and magma coexist as a two-phase aggregate in which the solid grains of rock form a viscously deformable framework or matrix. Liquid magma resides within the permeable network of pores between grains. Deviatoric stress causes the distribution of contact area between solid grains to become anisotropic; this, in turn, causes anisotropy of the matrix viscosity at the continuum scale. In the second of a two-paper set, we use numerical methods to solve the full, nonlinear, time-dependent equations governing this system. We consider porosity evolution in simple shear, Poiseuille and torsional flow. Under viscous anisotropy, there are two modes of porosity evolution: base-state segregation, which modifies the domain-scale porosity distribution, and growth of porosity perturbations into melt-rich bands. Simulation results with fixed anisotropy confirm and extend the linearized analysis of Part 1 (Takei & Katz, *J. Fluid Mech.*, vol. 734, 2013, pp. 424–455). Most importantly, numerical solutions capture the interaction of the two modes: under Poiseuille flow, base-state segregation enhances band formation; under torsional flow, bands are suppressed. Simulations also show that low band angle is maintained by nonlinear processes such as reconnection of high-porosity segments and by back-rotation of the compacted regions between bands. Simulations with dynamic anisotropy modify these results, further lowering the average band angle. The effective viscosity of each flow is controlled by base-state segregation; it does not evolve under simple shear, decreases in Poiseuille flow and increases in torsion. We propose a reinterpretation of experimental results in terms of the consequences of viscous anisotropy.

Key words: complex fluids, geophysical and geological flows, Stokesian dynamics

1. Introduction

Segregation of magma from the partially molten mantle is of interest to Earth scientists as a process that controls volcanism and, over Earth history, the chemical differentiation of the planet. Modelling this process is a problem in two-phase fluid dynamics: the flow of a low-viscosity liquid (magma) through the pores of a viscously deformable, permeable, solid matrix (rock). In Takei & Katz (2013), the first part

† Email address for correspondence: richard.katz@earth.ox.ac.uk

of this two-paper set, we reviewed and extended a relatively new theory for two-phase dynamics of a partially molten aggregate. This theory incorporates a tensorial, anisotropic viscosity for deformation of the two-phase system; its properties are derived from a microscale analysis in which the solid grains deform by diffusion creep (Takei & Holtzman 2009*a*,*b*). The companion paper (Part 1) demonstrates the fundamental consequences of viscous anisotropy on the porosity evolution of a deforming, partially molten rock by analysing the linearized governing equations. This linear analysis computes the growth of infinitesimal, periodic perturbations to a uniform background state; it is formally restricted to small strains at the onset of instability, when higher-order or nonlinear effects can be neglected. Relevant laboratory experiments on partially molten rocks, however, produce an anastomosing network of high-porosity bands that develops and persists over large strains (Kohlstedt & Holtzman 2009). This observation suggests that nonlinear processes are essential to the evolution of the system. In this paper, we present numerical solutions to the fully nonlinear, time-dependent governing equations.

Our present goals are to examine the validity and limitations of the linearized analysis in Part 1, to develop a better understanding of the theory of two-phase flow with anisotropic viscosity (particularly for nonlinear processes), and to explore implications of the theory that are relevant to experiments. This should lead to a quantitative comparison with laboratory experiments in subsequent work.

The theory and boundary conditions that we consider are motivated by published laboratory experiments on partially molten rocks. Schematic diagrams of two experimental configurations with images of experimental products are shown in figure 1 of Part 1. They are performed on synthetic rocks created by combining microscopic grains of the mineral olivine with a powder of basaltic lava. In a typical experiment, a sample of this rock is loaded into a deformation apparatus where it is raised to high pressure and temperature, such that the basaltic component melts while the olivine grains remain solid. After statically annealing the mixture until it has reached a textural equilibrium that is nearly uniform throughout the rock, a load is applied, causing controlled deformation of the two-phase aggregate. When a specified strain is reached the experiment is quenched, freezing in the spatial distribution of liquid (basalt) and solid (olivine); then it is sectioned and analysed in terms of this porosity distribution. The key result that has been obtained under both simple shear (Holtzman *et al.* 2003) and torsional (King, Zimmerman & Kohlstedt 2010) deformation is the emergence of a pattern of high-porosity bands at a low angle ($\sim$15–20°) to the shear plane. This pattern is observed to persist to large shear strains. Other characteristics of the pattern such as band spacing and feedback on deformation of the aggregate have been documented. Despite theoretical work by Stevenson (1989) that predicted this category of pattern-forming instability, most of the characteristics of experimental results are without detailed, quantitative explanation.

Models of the patterns observed in experiments have typically postulated some form of isotropic viscosity of the aggregate, incorporated it into the governing equations, then applied linearized analysis and numerical simulations to generate quantitative predictions. Katz, Spiegelman & Holtzman (2006) considered a non-Newtonian viscosity of the solid phase and showed that the dominant angle at which high-porosity bands appear in simulations is controlled by the sensitivity of the viscosity to the strain rate; more strain-rate weakening gives rise to a smaller angle between bands and the shear plane. The laboratory experiments, however, produce low-angle bands

in both Newtonian and non-Newtonian deformation regimes (Kohlstedt & Holtzman 2009; King *et al.* 2010), which falsifies the hypothesis of Katz *et al.* (2006).

Anisotropic viscosity may provide an alternative explanation for low-angle bands. Support for this hypothesis comes from linearized analysis in Part 1, and in Takei & Holtzman (2009*c*) and Butler (2012); the latter also presented numerical solutions to the full governing equations including anisotropy. Motivated by observations of coherently aligned melt-pockets under deviatoric stress (Zimmerman *et al.* 1999; Takei 2010), Butler (2012) adopted the theory of Takei & Holtzman (2009*c*) and considered two orientations of the anisotropy tensor. For anisotropy arising from melt pockets perpendicular to the direction of least compressive stress, he obtained low-angle bands in both numerical solutions and linearized analysis, consistent with laboratory experiments. For anisotropy arising from melt pockets aligned at 20° to the shear plane (Zimmerman *et al.* 1999), however, he found high-angle melt bands that are inconsistent with experiments. Butler (2012) considered only simple-shear deformation, however, and imposed a static anisotropy, rather than allowing it to evolve according to the dynamics. Moreover, to develop a more complete understanding of the consequences of viscous anisotropy, it is crucial to consider flows with a large-scale gradient in shear stress. This is not the case for simple shear.

Here we present a larger set of simulation results and a more thorough analysis of their behaviour. We consider the three deformation geometries that were analysed in Part 1: simple shear and Poiseuille flow in two spatial dimensions, and torsional flow in three dimensions. In discussing the results of numerical simulations, we invoke concepts and terms introduced for the linearized analysis. For example, the concept of base-state flow is used below. As in Part 1, base-state flow refers to the motion of both solid and liquid that occurs for a porosity field that is uniform at $t = 0$. We also discuss simulations in terms of the growth rate of perturbations; while these concepts have a clear mathematical definition in the context of stability analysis, their meaning here is less precise, although it is equally useful. The reader is encouraged to obtain (at least) a qualitative understanding of the results in Part 1 before continuing with the present paper.

This paper is organized as follows. In § 2 we review the formulation of the governing equations, viscosity tensor, and boundary conditions. We also discuss the discretization and approach to obtaining numerical solutions. This is followed by the results in § 3, where we first present a benchmark problem based on analytical solutions from linearized stability analysis. We then present results for simulations with fixed anisotropy, and simulations with dynamically evolving anisotropy. A discussion of the results is provided in § 4 and a condensed list of conclusions in § 5.

2. Formulation and solution of the numerical problem

The three deformation geometries that we consider are shown in figure 1. Under simple shear and parallel-plate Poiseuille flow, the system is assumed to be uniform in the Z direction, and we consider a two-dimensional domain in X and Y. The coordinate axes are aligned such that X–Z is the shear plane; this means that for Poiseuille flow, the body force (gravity) points in the $-X$ direction. Under torsional flow the domain is three-dimensional with an inherently periodic coordinate ψ, representing the angle around the cylinder.

As shown in figure 1, the domain for torsional flow has been modified from its form in Part 1. In particular, the radial span of the computational domain begins

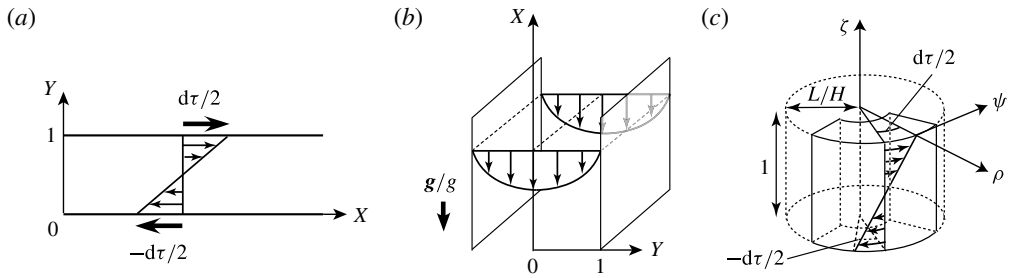

FIGURE 1. Three flow configurations considered in this study. Simple shear flow (*a*) and parallel-plate Poiseuille flow (*b*) are two-dimensional, while torsional flow (*c*) is three-dimensional. The domain for torsional flow, demarcated by solid lines, is a subregion of the cylinder used in Part 1.

at $\rho = \rho_0 > 0$ and the angular span is less than 2π rad. Both of these are chosen as a matter of computational convenience. For the former, this is because the grid is discretized in terms of the cylindrical coordinates and the tangential grid spacing $\rho\Delta\psi$ vanishes as the radial coordinate approaches zero. For the latter, the choice is simply to reduce computational cost at a given grid resolution.

All simulations begin with a uniform porosity ϕ_0 modified by a small perturbation $\epsilon\phi_1$. Our primary objective is to compute the evolution of this initial porosity field according to the equations describing conservation of mass and momentum in the two-phase aggregate.

2.1. *Governing equations, variables and boundary conditions*

A complete discussion of the governing equations is given in Part 1 and is not repeated here. In non-dimensional form, the equations are

$$\frac{\partial\phi}{\partial\tau} = \nabla\cdot[(1-\phi)\boldsymbol{V}], \tag{2.1}$$

$$\nabla\cdot\boldsymbol{V} = \frac{R^2}{r_\xi + 4/3}\nabla\cdot\left[\left(\frac{\phi}{\phi_0}\right)^n\nabla P\right], \tag{2.2}$$

$$P_{,i} = \left[C_{ijkl}\dot{e}_{kl}\right]_{,j}, \tag{2.3}$$

where the primary variables are porosity ϕ, mantle matrix velocity $\boldsymbol{V}$, and piezometric liquid pressure P (note that liquid/solid densities are assumed constant and equal; therefore, the gravitational body force is consequential only for Poiseuille flow). Also, τ is time, R is the compaction length, r_ξ is the ratio of the bulk and shear viscosities, n is a constant, $\dot{e}_{ij}$ is the matrix strain-rate tensor and C_{ijkl} is the viscosity tensor. For simple shear, time τ corresponds to the shear strain γ; for torsion, it corresponds to the total twist of the sample in radians. All symbols are dimensionless, although the asterisks introduced in the non-dimensionalization have been dropped. A version of (2.3) in cylindrical coordinates for torsional flow is given in appendix B of Part 1.

Equation (2.1) is a statement of conservation of mass for the matrix phase; equation (2.2) expresses a balance of stresses for the liquid phase; equation (2.3) is a stress balance for the solid + liquid aggregate. These balances are identical to the set considered by McKenzie (1984), except for the tensorial viscosity C_{ijkl}. The form of

this tensor is described in detail in Part 1. It is written as

$$C_{ijkl} = \mathrm{e}^{-\lambda(\phi-\phi_0)} \times \begin{array}{c} ij\downarrow \\ XX \\ \\ YY \\ \\ ZZ \\ YZ \\ ZX \\ XY \end{array} \begin{array}{c} kl\rightarrow \\ \\ \\ \\ \\ \\ \\ \\ \end{array} \begin{array}{cccccc} XX & YY & ZZ & YZ & ZX & XY \\ r_\xi + \frac{4}{3} & r_\xi - \frac{2}{3} & r_\xi - \frac{2}{3} & 0 & 0 & -\alpha\cos^3\Theta\sin\Theta \\ -\alpha\cos^4\Theta & -\frac{\alpha}{4}\sin^2(2\Theta) & & & & \\ \cdot & r_\xi + \frac{4}{3} & r_\xi - \frac{2}{3} & 0 & 0 & -\alpha\cos\Theta\sin^3\Theta \\ & -\alpha\sin^4\Theta & & & & \\ \cdot & \cdot & r_\xi + \frac{4}{3} & 0 & 0 & 0 \\ \cdot & \cdot & \cdot & 1 & 0 & 0 \\ \cdot & \cdot & \cdot & \cdot & 1 & 0 \\ \cdot & \cdot & \cdot & \cdot & \cdot & 1 - \frac{\alpha}{4}\sin^2(2\Theta) \end{array}, \tag{2.4}$$

where we have excluded (or replaced by dots) entries that, by symmetry of the tensor, are equal to those that are shown (e.g. the $XX\,YX$ entry). In the viscosity tensor, λ is a constant factor controlling the rate of weakening with increasing porosity; α is the magnitude of anisotropy, bounded between zero and two; and Θ is the anisotropy angle, the local direction of maximum tensile stress. Both the magnitude and angle of anisotropy may vary in space and time.

The anisotropy of diffusion creep viscosity described by (2.4) is a consequence of the distribution of melt and solid at the grain scale. Melt pockets between solid grains provide a fast pathway for diffusion of the solid in response to deviatoric stress. If these pockets are coherently aligned, the diffusivity (averaged over a volume containing many grains) becomes anisotropic (Takei & Holtzman 2009*a*), giving rise to directions that are more and less compliant to stress. A detailed discussion is provided in Part 1 and in Takei & Holtzman (2009*a*). Table 1 provides a list of selected notation and parameter values. Parameters α and Θ are treated as constants in the fixed-anisotropy calculations (§ 3.2) and as functions of local stress in the dynamic-anisotropy calculations (§ 3.3).

The above equations govern both the domain-scale shear of the mantle matrix and the compaction flow. The latter is a relatively smaller component of the velocity, but is of greater interest because it controls the porosity evolution. In simple shear and torsional flow, the dominant shear-flow pattern is imposed by the boundary conditions; it can be separated from the unknown part to isolate deviations. Hence, we define

$$\boldsymbol{U}(\boldsymbol{X},\tau) = \begin{cases} \boldsymbol{V} - \left(Y - \frac{1}{2}\right)\hat{\boldsymbol{e}}_X & \text{simple shear flow (Butler 2009)}, \\ \boldsymbol{V} - \rho\left(\zeta - \frac{1}{2}\right)\hat{\boldsymbol{e}}_\psi & \text{torsional flow}, \end{cases} \tag{2.5}$$

where $\hat{\boldsymbol{e}}_a$ is a unit-vector pointing in the a direction. Under Poiseuille flow, the background flow field is generated by the body force, rather than by the imposed boundary conditions and, hence, it depends on rheological parameters. Our numerical code for Poiseuille solves for the full matrix velocity $\boldsymbol{V}$.

	Symbol	Value (range)
Cartesian coordinates normalized to domain size	X, Y, Z	
Cylindrical coordinates normalized to domain size	ρ, ψ, ζ	
Primary field variables	$\boldsymbol{V}, \phi, P$	
Compaction length normalized to the domain size	R	0.1 or 1
Bulk/shear viscosity ratio (Takei & Holtzman 2009*a*)	r_ξ	5/3
Porosity weakening factor	λ	27
Porosity exponent for permeability	n	2
Anisotropy magnitude	α	2 (0–2)
Anisotropy angle (to the X–Z or ρ–ψ plane)	Θ	45°
Normalized saturation stress for anisotropy amplitude	σ_{sat}	2
Initial uniform porosity	ϕ_0	0.05
Initial amplitude of porosity perturbation	ϵ	0.01 (10^{-4}–10^{-2})

TABLE 1. Selected variables, parameters and representative values.

We can restate the boundary conditions using the modified velocity from (2.5) and the modified domain for torsional flow as

$$\text{Simple shear} \quad \begin{cases} U_X = 0, \;\; U_Y = 0, \;\; k_\phi = 0 & \text{at } Y = 0, 1, \\ \text{periodic} & \text{at } X = 0, X_{max} \end{cases} \tag{2.6a}$$

$$\text{Poiseuille} \quad \begin{cases} V_{X,Y} = 0, \;\; V_Y = 0, \;\; P_{,Y} = 0 & \text{at } Y = 0, \\ V_X = 0, \;\; V_Y = 0, \;\; k_\phi = 0 & \text{at } Y = 1, \\ \text{periodic} & \text{at } X = 0, X_{max} \end{cases} \tag{2.6b}$$

$$\text{Torsion} \quad \begin{cases} U_\rho = U_{\psi,\rho} = U_{\zeta,\rho} = 0, \;\; k_\phi = 0 & \text{at } \rho = \rho_0, L/H, \\ U_\rho = U_\psi = U_\zeta = 0, \;\; k_\phi = 0 & \text{at } \zeta = 0, 1, \\ \text{periodic} & \text{at } \psi = 0, \;\; \psi_{max}. \end{cases} \tag{2.6c}$$

Here we have reintroduced the dimensionless permeability k_ϕ. The reflection boundary conditions at $\rho = \rho_0, L/H$ in the torsion configuration are intended to allow compaction to occur at the inner and outer walls of the domain, consistent with experiments.

2.2. *Discretization and numerical solution*

The governing equations are discretized in space with a finite-volume method on a staggered mesh, and in time with a semi-implicit finite difference. For simple shear and Poiseuille simulations the mesh spacing is uniform, with spacing δ_X in both directions; for torsion, the mesh spacing is uniform in ρ, ψ and ζ and, hence, the tangential cell width and cell volume increase with radius ρ. The flux-divergence term in (2.1) is discretized with a second-order, Fromm upwind-advection scheme (Trompert & Hansen 1996). The discretization results in a system of nonlinear algebraic equations that are solved iteratively using Newton's method. The update at each iteration is computed for the two-dimensional problems with a direct solver (MUMPS: MUltifrontal Massively Parallel sparse direct Solver; see Amestoy *et al.* (2001)) and, for the torsional flow case, with an incomplete LU-preconditioned, iterative Krylov scheme (Cai, Keyes & Venkatakrishnan 1997).

The size of the time step is determined according to a Courant–Friedrichs–Lewy condition on the matrix velocity. At each time step, the tensorial viscosity field is calculated using the porosity ϕ and anisotropy fields α and Θ from the previous time step (or that are fixed as parameters). Equations (2.2) and (2.3) are then solved as a coupled system for pressure and velocity. Finally, the porosity is updated using the discrete conservation of mass equation (2.1). Lagging the anisotropy calculation as described is an approximation that reduces computational cost and improves robustness of convergence. A more rigourous treatment includes α and Θ as field variables that are solved together with $\boldsymbol{V}$ and P; a comparison of this approach with the lagged approximation under simple shear produces differences that are negligible relative to the common variations.

All software for the present applications is implemented within the framework of the Portable, Extensible Toolkit for Scientific Computation (PETSc) (Balay *et al.* 2001, 2004; Katz *et al.* 2007).

3. Results

Results are reported in three subsections below: benchmark calculations § 3.1, simulations with fixed anisotropy § 3.2 and simulations with dynamic anisotropy § 3.3.

3.1. *Code benchmarks*

Two benchmark calculations assess the convergence and accuracy of numerical solutions for simple-shear flow. The Poiseuille and torsional flow codes are not benchmarked, but they use the same algorithms and share many subroutines with the simple shear code.

The benchmark computations solve for the growth of a single mode of sinusoidal perturbation with a specified wavelength and angle to the shear plane. They are performed on a unit-square domain with boundary conditions (2.6*a*) and 400×400 grid cells; they use anisotropy parameters $\alpha = 2$ and $\Theta = 45°$, dimensionless compaction length $R = 0.2$ and viscosity ratio $r_\xi = 5/3$. The benchmarks consider only the instantaneous growth rate, computed at a maximum in porosity as $\dot{s} = (1 - \phi)\nabla \cdot \boldsymbol{V}/\epsilon$, where ϵ is set to be 10^{-4} (see (5.16) in Part 1, with $\phi_1 = 1$). This diagnostic calculation is applied to a small patch in the centre of the domain that is isolated from the boundary conditions by virtue of its distance from them in compaction lengths. The result is compared with the linearized stability analysis, (5.17) of Part 1.

Figure 2 presents the results of both benchmarks. Figure 2(*a*) compares the numerical and analytical growth rates for different wavelengths of perturbation at a constant perturbation angle $\theta = 15°$. The x-axis is cast in terms of the number of grid cells per perturbation wavelength, a measure of the grid resolution. The figure shows that below $\sim$15 grid cells per wavelength, the numerically computed growth rate is significantly less than the analytical value. We therefore expect that the numerics will damp smaller-wavelength modes that are insufficiently resolved by the grid, but will accurately capture larger-wavelength modes. Figure 2(*b*) compares the numerical and analytical growth rates for all perturbation angles θ using a grid with 40 cells per perturbation wavelength. Evidently the solution accuracy is independent of θ.

These benchmark results validate the solution of (2.2) and (2.3) under simple-shear deformation. They do not validate the solution of (2.1), which involves discretization of the divergence of the solid flux. That equation, however, is solved using previously tested subroutines (Katz *et al.* 2006, 2007). Furthermore, while the code used to model Poiseuille flow is nearly identical with the simple-shear code, the code for torsional

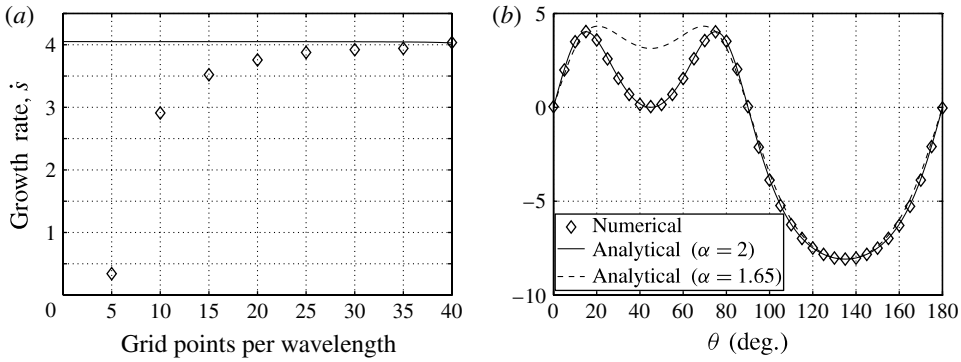

FIGURE 2. A comparison between perturbation-growth rate at $\tau = 0$, as computed numerically (symbols) and analytically (lines) for simple shear. Calculations use anisotropy parameters $\alpha = 2$ and $\Theta = 45°$, dimensionless compaction length $R = 0.2$, and bulk viscosity ratio $r_\xi = 5/3$. (*a*) Growth rate as a function of the number of grid-cells per wavelength of the initial perturbation ($\theta = 15°$). Wavelengths range from $1/80$ to $1/10$. (*b*) Growth rate as a function of the perturbation angle θ for perturbation wavelength $1/10$ using 40 grid cells per wavelength. The $\alpha = 1.65$ curve is for reference below.

flow is substantially different. The present benchmarks support the validity of this latter code, but are not conclusive. A variety of informal tests indicate that the code for torsional flow is correctly implemented.

3.2. *Fixed anisotropy*

The governing equations prescribe an anisotropy tensor that is a function of the instantaneous state of stress, and hence should evolve with the changing porosity field. To simplify the analysis and facilitate comparison with results from Takei & Katz (2013), consideration is first given to numerical solutions in which the anisotropy tensor is calculated using fixed values of α and Θ (material parameters are given in table 1). We consider alignment at $\Theta = 45°$ only, consistent with Takei & Katz (2013); this is the angle that arises from the base-state flow regime. We explore the consequences of different values of anisotropy magnitude α and compaction length R.

Simulations are initialized with a porosity field $\phi(\boldsymbol{X}, \tau = 0) = \phi_0 + \epsilon\phi_1(\boldsymbol{X})$, where $\epsilon < \phi_0$ is a constant and $|\phi_1| \leqslant 1$ is a random perturbation, generated by spectral filtering of uniformly distributed white noise. The filter sets to zero all Fourier modes with a wavelength less than $15\delta_X$.

3.2.1. *Simple shear flow*

Figure 3 shows the porosity field at four successive times in a representative simple-shear simulation. This calculation uses saturated anisotropy $\alpha = 2$ with a reference compaction length R that is one-tenth the height of the domain; other parameter values are given in table 1. Figure 3(*a*) is the initial condition, which is the same used for each simple-shear simulation. In figure 3(*b,c*) the pattern of low-angle, high-porosity bands emerges from the background noise. Figure 3(*d*) shows that with progressive strain, the bands become enriched in melt and the regions between bands are compacted to vanishingly small porosity.

The angle that high-porosity bands make with the shear plane is an important characteristic of simulation results; it has been the focus of previous studies, both

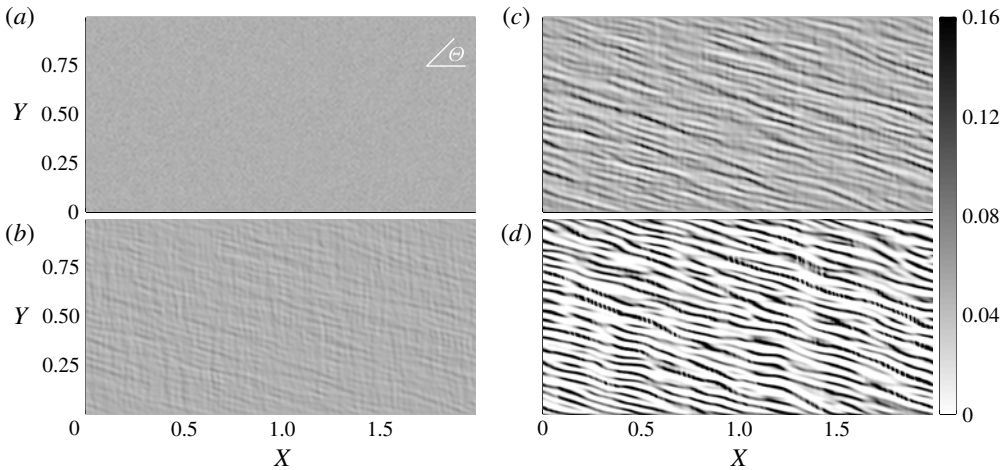

FIGURE 3. Simple-shear flow. A representative simulation with magnitude of anisotropy $\alpha = 2$ and non-dimensional compaction length $R = 0.1$. Grid size is 1200×600. Each figure is labelled with its value of total strain γ and its minimum and maximum porosity. Compare with figure 3(*b*) of Butler (2012), who used a grid resolution that is coarser by a factor of 50: (*a*) $\gamma = 0.0$, $\phi \in [0.04, 0.06]$; (*b*) $\gamma = 0.5$, $\phi \in [0.03, 0.07]$; (*c*) $\gamma = 1.0$, $\phi \in [0.00, 0.26]$; (*d*) $\gamma = 1.5$, $\phi \in [0.00, 0.96]$.

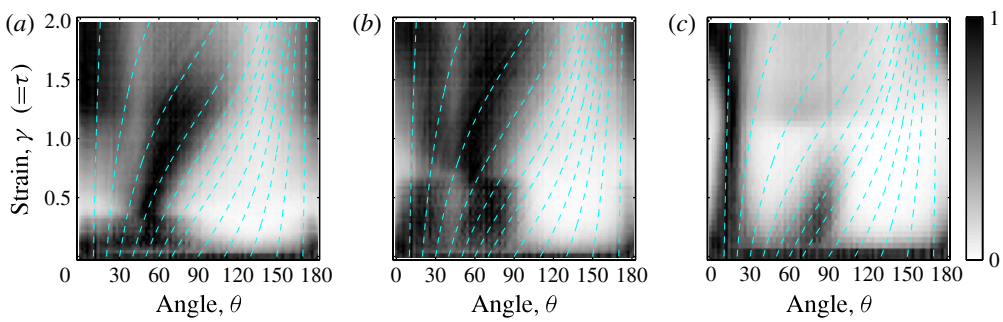

FIGURE 4. (Colour online) Spectral evolution diagrams for three simulations with $R = 0.1$ and other parameters as in table 1. Greyscale indicates spectral amplitude; curves are passive advection trajectories (see the main text). Simulation grid size is 1200×600. Each figure represents a different value of α: (*a*) $\alpha = 0$; (*b*) $\alpha = 1.5$; (*c*) $\alpha = 2$. The spectral evolution for the simulation shown in figure 3 is given in (*c*).

experimental (Kohlstedt & Holtzman 2009) and theoretical (Spiegelman 2003; Katz *et al.* 2006; Takei & Holtzman 2009*c*; Butler 2012). To quantify the distribution of band angles in simulations, we follow the approach of Katz *et al.* (2006) and introduce an angular amplitude spectrum. This is computed by summing the output of a two-dimensional discrete Fourier transform $\mathscr{F}_{ij}$ in finite bins; each bin is defined by a range of angles of the wavevector. Figure 4 shows, in the greyscale images, the evolution of these angular spectra with progressive strain, for a suite of simulations with different values of α, at fixed R. At each increment of strain γ, the spectrum has been scaled by its maximum value and shaded according to amplitude. The

dashed curves are passive advection trajectories (Katz *et al.* 2006); each represents the evolving angle between the shear plane and a material line that is passively embedded within a simple-shear flow.

At $\gamma = 0$, the spectral amplitude is independent of angle, consistent with an initial noise field that is isotropic. The linearized analysis from Part 1 indicates that at finite strains much less than one, features emerge from the noise according to a growth rate that depends on their angle to the shear plane. For $\alpha = 2$, the linearized analysis predicts symmetric peaks in the growth rate of perturbations at $\sim 15°$ and $\sim 75°$. The angular spectrum in figure 4(*c*) reflects this; at $\gamma = 0.25$ there is clearly spectral power at both growth peaks. Figures 3 and 4 show that the high-angle features persist to $\gamma = 0.5$ but decay rapidly after that. Figure 4(*a,b*) are also qualitatively consistent with predicted growth rates from linearized analysis at early times.

The symmetry between high- and low-angle features is broken by their different rates of rotation in the background, simple-shear flow. Passive advection trajectories in figure 4 show that high-angle features are rapidly rotated away from orientations favourable for growth, while low-angle features experience slow or negligible rotation. This helps to explain why low-angle bands produced in simulations with $\alpha = 2$ are stable up to large strains: their orientation is least affected by passive advection in the background flow.

Although some trends of the spectral evolution in figure 4 are parallel to the passive advection trajectories, significant deviations also exist: in figure 4(*a*), a dark lobe appears at $\gamma \approx 1$ and $\theta \lesssim 30°$, $\theta \gtrsim 170°$ (note that the θ axis in this figure is periodic); in figure 4(*b*), there is a break in the pattern of growth at about $\gamma = 0.75$; in figure 4(*c*), the low-angle lobe trends toward 0° for $\gamma > 1.25$. One reason for these deviations is that the porosity field is reorganized by differential flow of liquid and solid. This nonlinear process of reconnection operates such that low-angle features grow at the expense of high-angle features (Holtzman, Kohlstedt & Morgan 2005); it is especially relevant in figures 3 and 4(*c*). Numerical simulations by Katz *et al.* (2006) demonstrated the reconnection mechanism for maintaining bands at low angle under isotropic viscosity.

Low band angles are also maintained by localization of the overall shear deformation onto narrow, weak zones. Figure 5 shows the perturbation vorticity $(\nabla \times \boldsymbol{U}) \cdot \hat{\boldsymbol{e}}_z$ at a strain of 1, corresponding to the porosity field in figure 3(*c*). Regions of high porosity correspond with enhanced shear; this is consistent with exponential weakening due to melt localization. As differential flow of liquid and solid drives the porosity contrast upward, strain becomes increasingly localized onto the mechanically weak bands. To maintain compatibility with the boundary conditions, the integral of the perturbation vorticity over the domain must vanish and, hence, the compacted regions between bands must have perturbation vorticity greater than zero. Positive values of $(\nabla \times \boldsymbol{U}) \cdot \hat{\boldsymbol{e}}_Z$ in figure 5 represent areas of reduced rotation; since the non-dimensional background vorticity of simple shear is -1, a perturbation vorticity > 1 represents counter-rotation. Vertical white stripes in figure 5 are stacks of compacted blocks with diminished vorticity; they give rise to the sigmoidal shape of some bands in figure 3(*d*). The partitioning of vorticity helps to explain the spectral evolution in figure 4(*c*) for $\gamma > 1.25$; spectral amplitude at angles less than 10° grows as a consequence of reconnection and counter-rotation of bands.

Despite the complexities arising from interacting Fourier modes and nonlinear evolution of the system, figure 6 shows that the growth rate of the dominant Fourier mode remains close to that predicted by linear analysis over a large interval in strain.

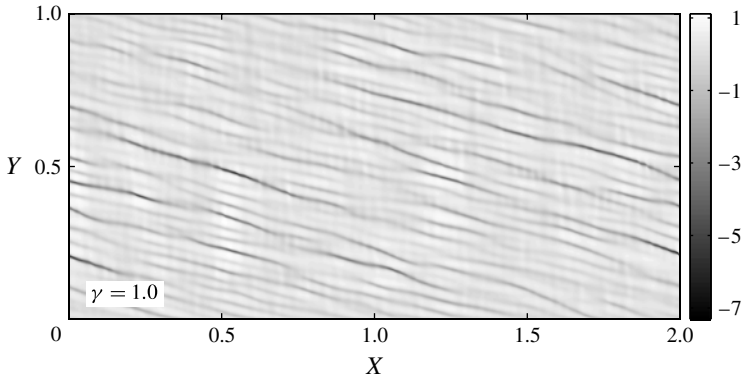

FIGURE 5. Perturbation vorticity $(\nabla \times \boldsymbol{U}) \cdot \hat{\boldsymbol{e}}_Z$ at $\gamma = 1$ with $\alpha = 2$, corresponding to the porosity field in figure 3(*c*). Discrete integration of this field over the domain gives $\sim 10^{-6} \approx 0$. The vorticity of the background simple-shear flow is -1 and hence from (2.5), the full vorticity is $(\nabla \times \boldsymbol{V}) \cdot \hat{\boldsymbol{e}}_Z = (\nabla \times \boldsymbol{U}) \cdot \hat{\boldsymbol{e}}_Z - 1$.

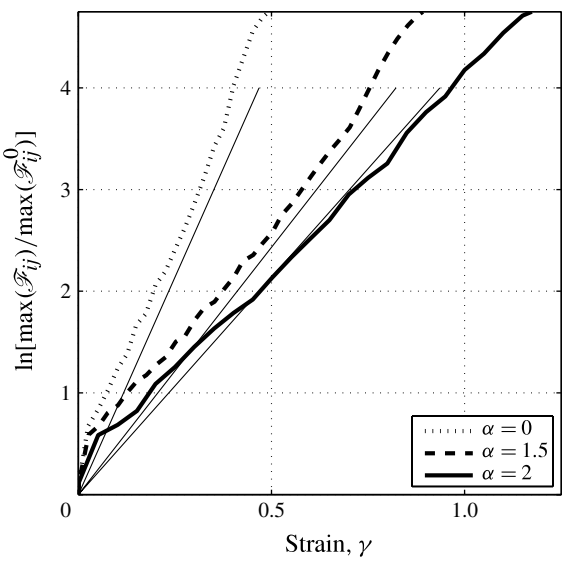

FIGURE 6. Log-amplitude of the largest Fourier mode as a function of progressive strain, from simulations with three values of α, normalized by the maximum Fourier amplitude of the initial noise field. Narrow lines represent the predictions from linearized stability analysis.

At sufficiently large strains, high-porosity bands in simulations draw melt lengthwise toward their centres until they form an array of approximately equant melt pools with porosity at or near unity. These pools of melt are advected with the solid flow.

3.2.2. *Poiseuille flow*

Poiseuille flow with anisotropic viscosity presents a complexity that is not present under simple shear: there are three distinct but interacting modes of liquid segregation. The most fundamental of these is caused by the gravitational body force; it is independent of the anisotropy of the two-phase mixture. The body force acts on both

phases, drawing the liquid downward more rapidly than the solid (see appendix C.2 of Part 1). Initially, when the porosity is uniform, this gravity-driven segregation is purely vertical.

The background deformation field of the solid phase simultaneously drives the two other modes of segregation. The first of these is localization into high-porosity bands, as also occurs under simple shear. In fact, over any sufficiently small patch of the domain, the solid flow pattern is approximately equal to simple shear. The second mode is liquid segregation over the full width of the domain, moving up the stress gradient toward the no-slip boundary. Borrowing terminology from linearized analysis, the latter mode will be referred to as base-state segregation because it operates irrespective of perturbations to the background Poiseuille flow, while the former will be referred to as porosity-band formation. Each of these modes have different length scales of segregation, and each proceeds at a different rate.

Linearized stability analysis treats each of these modes of liquid segregation separately by computing their respective rates of growth at $\tau = 0$. In contrast, numerical simulations are not constrained to track any individual mode, and hence capture the full evolution of the porosity field over finite strains. Figure 7 shows snapshots of the porosity from simulations with two different values of the compaction length R and three different values of α. All simulations start with the same smoothed-noise perturbation at amplitude $\epsilon = 0.01$. High-porosity bands for $\alpha = 0$ and $\alpha = 2$ are coherently aligned at angles consistent with predicted growth rates. The case of $\alpha = 1.5$ is more complex: high porosity features are oriented at angles greater than 45° to the shear plane, but are arrayed along lines at less than 45°. Similar behaviour is seen for $\alpha = 1.5$ in simple-shear simulations.

A closer examination of simulation results in figure 7 reveals evidence for base-state segregation, and confirms that it is sensitive to R, the size of the compaction length relative to the width of the domain. Curves plotted at the top of each panel represent the vertically averaged porosity $\overline{\phi}(Y)$ and vertically averaged X component of the velocity $\overline{v_X}(Y)$ (see the figure caption for details). The averaged-porosity curves in figure 7(*a,d*) (for isotropic viscosity $\alpha = 0$) have only small deviations from $\overline{\phi}(Y) = \phi_0$ because without anisotropy, there is no coupling between σ_{XY} and $\dot{e}_{YY}$. In contrast, figure 7(*b,c,e,f*) have $\alpha > 0$ and should exhibit base-state segregation. The $\overline{\phi}(Y)$ curves show that this is indeed the case; they also show that the strength of base-state segregation increases with R. For $R = 0.1$, base-state compaction and decompaction are limited to boundary layers at $Y = 0, 1$ that have a width approximately equal to the compaction length. For $R = 1$, the compacting and decompacting regions together span the domain in the Y direction. The resultant segregation is apparent in the greyscale gradient along this span (figure 7*e,f*).

Base-state segregation affects the magnitude of the shear-strain rate $\dot{e}_{XY}$ under Poiseuille flow, where the dominant stress balance is between the body force and the shear stress transmitted from the no-slip domain wall. Liquid segregation toward the wall reduces the viscosity there, requiring ever-larger shear-strain rates to maintain this stress balance. A comparison of dashed curves in figure 7(*c,f*) shows that greater base-state segregation at larger R produces faster downward flow of the two-phase aggregate.

Furthermore, figure 7 shows that growth of porosity bands is overprinted on the base-state segregation. Simulations with $\alpha = 2$ in figure 7 show that over finite strain, porosity bands grow faster for larger compaction length (note that figure 7(*c*) is a snapshot at $\tau = 1.1$, while figure 7(*f*) is at $\tau = 0.36$). This difference can be partially explained by the contrasting growth rates predicted by linearized analysis for $R = 1$

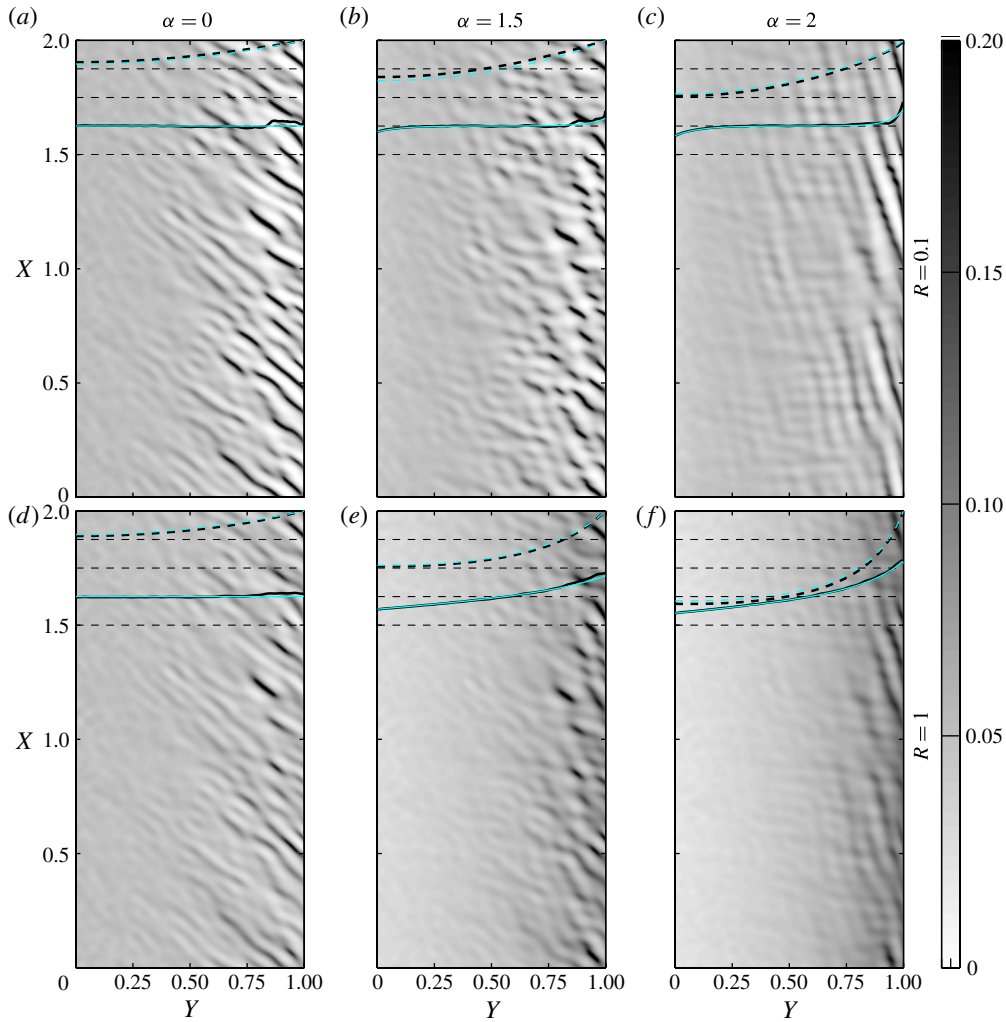

FIGURE 7. (Colour online) Poiseuille flow with a symmetry boundary on the left and a no-slip boundary on the right; gravity pulls in the $-X$ direction. Snap-shots from six simulations with different values of R (rows) and different values of α (columns). Greyscale shows the porosity. Simulation grid size is 500×1000. At the top of each figure are plots of vertically averaged porosity ($\overline{\phi}(Y)$, solid lines) and vertically averaged X component of solid velocity ($\overline{v_X}(Y)$, dashed lines). Thick lines are from the simulations shown; thin lines (shown in cyan online) are from a corresponding set of simulations with zero porosity perturbation, $\epsilon = 0$. Horizontal dashed gridlines represent $(0, 1, 2, 3) \times \phi_0$ for the porosity curves and $-(4, 3, 2, 1) \times 0.3$ for the vertical-velocity component, from bottom to top. The model time τ of each figure is chosen such that the images depict an approximately equal span of porosity: (*a*) $\tau = 1.1$; (*b*) $\tau = 1.1$; (*c*) $\tau = 1.1$; (*d*) $\tau = 0.8$; (*e*) $\tau = 0.5$; (*f*) $\tau = 0.36$.

and $R = 0.1$, shown in figure 9(*e,h*) of Part 1. However, the larger part of this difference is a consequence of the nonlinear dynamics, including interaction between base-state segregation and perturbation growth.

Figure 8 illustrates the interaction between base-state segregation and porosity band growth. The amplitude of porosity bands is quantified as the standard deviation of

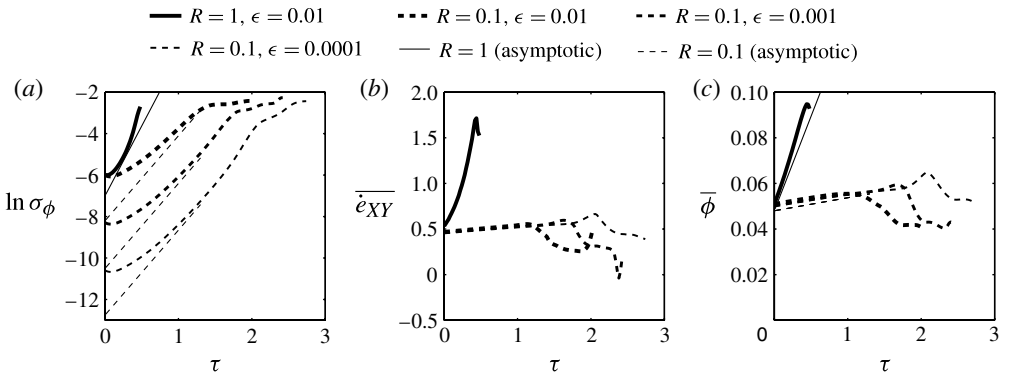

FIGURE 8. Evolution of the Poiseuille system at $Y = 0.9$ for four simulations with different values of R and ϵ (see the plot legend for details). (*a*) The logarithm of the standard deviation of porosity taken along vertical lines σ_ϕ. Curves from simulations are compared with linear trends having slope $\dot{s}$ from stability analysis (figures 9(*e*,*h*) of Part 1); the intercept of these trends is arbitrary. The calculation of $\dot{s}$ assumes $\theta = 15°$ and other parameters as in table 1. (*b*) The vertically averaged shear-strain rate. (*c*) The vertically averaged porosity. Asymptotic lines are computed with the base-state compaction rate, equations (5.8) and (C.2) of Part 1.

porosity σ_ϕ for a column of grid cells. Curves in figure 8(*a*) show $\ln \sigma_\phi$ at $Y = 0.9$; the logarithm is plotted because we expect porosity band amplitude to grow exponentially, based on linearized stability analysis. Exponential growth would appear as linear trends on this plot, as it does in figure 6 for simple shear. Predicted growth-rate trends from linear stability analysis are plotted as thin lines; these should parallel the simulation trends at $\tau \ll 1$. Deviation from the linear-stability trend is evident at early times for both large and small compaction length. The initial growth rate of bands is smaller than predicted under the frozen-time assumption of linearized analysis; this is probably a consequence of base-state segregation homogenizing small porosity variations by lateral redistribution of liquid.

At larger τ in figure 8(*a*), the slope of the $R = 1$ curve exceeds the trend from linearized analysis. This super-exponential growth is caused by the progressive localization of shear strain toward the no-slip wall. The shear-strain rate at $Y = 0.9$ is shown in figure 8(*b*). This localization of shear strain is, in turn, due to the reduction in viscosity associated with base-state segregation of liquid. Figure 8(*c*) shows the vertically averaged porosity $\overline{\phi}$ at $Y = 0.9$. It increases with time as base-state segregation drives liquid toward the no-slip wall. The increase of the $R = 1$ curve is more rapid than predicted by (linearized) base-state segregation, which is likely the consequence of interaction between modes. Low-angle, high-porosity bands become high-permeability conduits for gravity-driven segregation, directing liquid toward the wall. While the orientation of these conduits makes them favourable for gravity-driven segregation, it does not promote base-state segregation and may, in fact, inhibit it. Therefore, the steeper slope for $R = 1$ in figure 8(*c*) might be attributed to the combined effect of porosity-band formation and gravity-driven segregation on base-state segregation. The break in slope of curves in figure 8(*c*) is a consequence of localization of decompaction and shear into a layer of thickness less than 0.1 from the wall boundary.

Taken together, the evolution of parameters shown in figure 8 documents the nonlinear interaction between base-state and gravity-driven segregation, strain

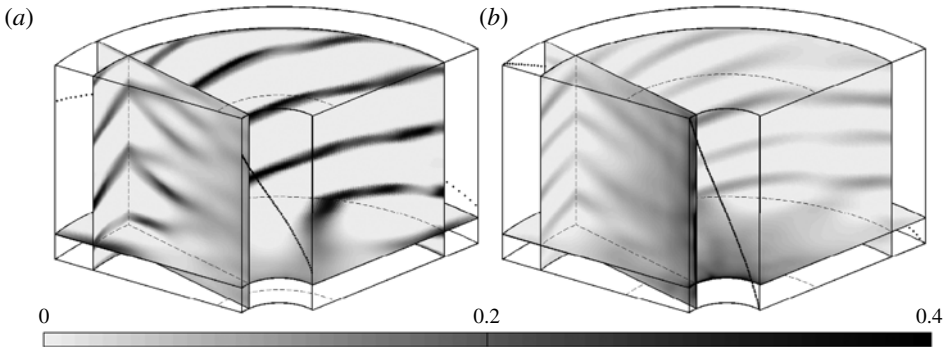

FIGURE 9. Three-dimensional rendering of sections through the porosity field from two simulations of torsional flow with $\alpha = 2$ and different values of R: (*a*) $R = 0.1$, $\tau = 3$; (*b*) $R = 1$, $\tau = 1.85$. Solid black lines enclose the computational domain; dashed black lines show the radius where the base-state shear strain in a ψ–ζ plane is unity; dotted black lines indicate total base-state strain at the inner- and outer-radius faces of the domain. Grid size is $150 \times 150 \times 150$.

localization and growth of porosity bands. The interaction shown in figure 8 is larger for $R = 1$ than for $R = 0.1$; this is primarily because base-state segregation and gravity-driven segregation ($\propto R^2$, appendix C.2 of Part 1) are both sensitive to the normalized compaction length.

3.2.3. *Torsional flow*

Torsional flow has similarities with both simple shear and Poiseuille flow: a cylindrical slice through the torsion domain at constant radius ρ has a background solid flow that is effectively a simple shear; like Poiseuille flow, it has base-state segregation arising from viscous anisotropy, even in the absence of porosity perturbations. However, torsional flow presents a further complication over Poiseuille flow, in that the dynamics are inherently three-dimensional. This complication means that numerical solutions for torsional flow necessarily incur a higher computational cost at similar spatial resolution. To make simulation of torsional flow feasible, we reduce the spatial resolution and truncate the domain to $(0, z_{max}) \times (\rho_0, L/H) \times (0, \psi_{max}) = (0, 1) \times (0.2, 1.2) \times (0, \sim 107°)$.

Figure 9 shows representative porosity-field output from two simulations of torsional flow with saturated anisotropy, $\alpha = 2$. These models have different compaction lengths and are presented at different amounts of twist τ. These two models are run with a grid size of $150 \times 150 \times 150$ cells within the domain, which is substantially coarser than simulations of simple shear and Poiseuille flow, above. Coarse grid resolution relative to the scale of perturbations (§ 3.1) and to the compaction length reduces the growth rate and increases the wavelength of the porosity-band instability. Despite this, simulations clearly exhibit the emergence of a banded structure of high and low porosity, similar to that observed in experiments (King *et al.* 2010).

In Part 1 we showed that at $\tau = 0$, base-state segregation for torsional flow drives liquid toward the centre of the cylinder, where shear stresses are smaller. Figure 9 confirms that this prediction is consistent with numerical solutions at finite strain. The relative rates of base-state segregation and porosity-band formation change with the size of the compaction length. Figure 9(*a*), with $R = 0.1$, has slower base-state segregation and, hence, porosity variations are dominated by flow into bands. In

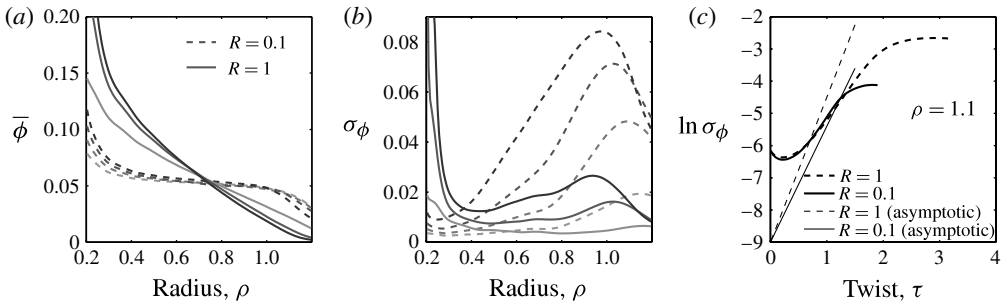

FIGURE 10. Profiles through two torsion simulations with $R = 0.1$ and $R = 1$. (*a*) The mean porosity $\overline{\phi}$, averaged over height ζ and angle ψ, as a function of radius. Darker lines indicate larger amounts of twist. Dashed lines for $R = 0.1$ at twist $\tau = 1.5,\ 2,\ 2.5,\ 3$ rad; solid lines for $R = 1$ at twist $\tau = 1,\ 1.5,\ 1.85$ rad. (*b*) The standard deviation of porosity σ_ϕ, taken over height and angle, as a function of radius. Line colour and style are as in (*a*). (*c*) The standard deviation of porosity on the $\rho = 1.1$ surface, as a function of twist τ. Thin lines show trends from stability analysis, computed assuming $\theta_\ell = 15°$ at $\ell = 1.2$; the intercept of these linear trends is arbitrary.

contrast, figure 9(*b*) with $R = 1$ displays strong radial variation in porosity with only weak bands, a consequence of base-state segregation. This is consistent with Poiseuille flow and figure 7, where larger compaction length was associated with enhanced base-state segregation.

As with Poiseuille flow, the relative amounts of base-state segregation and porosity-band formation can be quantified with the average and standard deviation of porosity, respectively. For torsional flow, we define $\overline{\phi}(\rho)$ as the average porosity in a ψ–ζ plane, as a function of radius ρ; similarly, the $\sigma_\phi(\rho)$ represents the standard deviation of porosity within the ψ–ζ plane, as a function of ρ. Figure 10 plots $\overline{\phi}$ (figure 10*a*) and σ_ϕ (figure 10*b*) for the same simulations shown in figure 9. Darker lines represent profiles computed for larger values of twist τ. The evolution of porosity due to base-state segregation is evident in figure 10(*a*): with increasing twist, compaction occurs at distal radii while decompaction occurs at proximal radii. For $R = 0.1$, (de)compaction occurs in boundary layers near the domain boundaries; for $R = 1$, these boundary layers together span the full radius of the domain.

The direction of base-state segregation introduces an important difference between torsional and Poiseuille flow. In torsional flow, base-state segregation transfers liquid away from distal radii toward the centre of the cylinder. Here $\dot{e}_{\psi\zeta}$ is larger at distal radii and hence this is where porosity-band growth should be faster. Figure 10(*b*) maps the amplitude of porosity perturbations σ_ϕ, as a function of radius and at different times. The dashed lines corresponding to $R = 0.1$ show strong band growth at distal radii, while solid lines for $R = 1$ show the largest porosity variation at proximal radii. (Fourier analysis described below demonstrates that the proximal variations for $R = 1$ do not take the form of coherently oriented bands.) This contrasting behaviour for different compaction lengths is a consequence of the redistribution of porosity by base-state segregation.

The time-dependence of σ_ϕ profiles in figure 10(*b*) reveals an interaction between base-state segregation and band growth. With increasing τ, the local maximum in σ_ϕ moves toward smaller ρ, even though the strain rate $\dot{e}_{\psi\zeta}$ increases outward. The inward migration of the peak in porosity variations is due to base-state segregation,

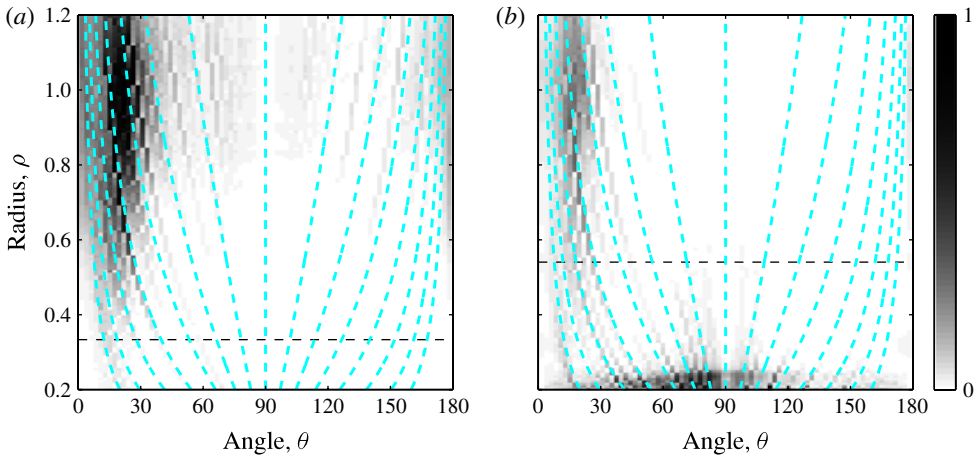

FIGURE 11. (Colour online) Fourier analysis of the output from torsional simulations shown in figure 9: (*a*) $R = 0.1,\ \tau = 3$; (*b*) $R = 1,\ \tau = 1.85$. Dashed lines show the variation of band angle with radius under the 'spiral staircase' assumption, used by Takei & Katz (2013) for linearized stability analysis. The angular spectrum at each radius is computed according to the approach used above for simple shear (§ 3.2.1) on a two-dimensional field $\phi(\psi, \zeta)$ that has been interpolated for equal grid spacing in the tangential and vertical directions. Horizontal dashed lines indicate the radius of the cylinder on which the background shear strain is unity.

which is associated with inward flow of liquid through the high-permeability bands toward small ρ. This diminishes the porosity variation σ_ϕ at large ρ. In comparison with Poiseuille flow, where base-state segregation enhances porosity-band growth (figures 7 and 8), torsional flow gives rise to a competition between porosity-band growth and radial, base-state segregation.

The effect of this competition is also evident in figure 10(*c*), which shows the evolution of the proxy for porosity band amplitude σ_ϕ at fixed radius $\rho = 1.1$. The curves from simulations are compared with linear trends from stability analysis. In contrast with figure 6 for simple shear but similar to results for Poiseuille in figure 8, the curves derived from simulations are not simply parallel to the trends from stability analysis. At small times, the amplitude of porosity perturbations decreases due to compaction and porosity homogenization by base-state segregation. With increasing τ, the growth of porosity perturbations accelerates, but it never reaches the slope predicted by stability analysis. Since $\overline{\dot{e}_{\psi\zeta}}$ is effectively constant, it cannot explain this deviation. Instead it can be attributed to the competing effect of base-state segregation. Furthermore, base-state segregation may be enhanced by the emergence of bands, which could act as high-permeability channels to transport melt from distal to proximal radii; the levelling of curves in figure 10(*c*) at large τ may be an expression of this nonlinear interaction.

Figure 11 provides information about the orientation of porosity variations evident in figure 9. It shows angular spectra computed by discrete Fourier transform at successive radial sections. Each radial section has a flow geometry that is like simple shear, wrapped around a cylinder. If each section were independent of the others, we would expect the spectral distribution to be about the same at every radius; this would predict constant-θ trends of angular amplitude in figure 11. Each radial section is, however, tightly coupled to its neighbours. We might therefore expect porosity to be

exactly constant in the radial direction. A banded porosity structure consistent with this assumption takes the form of a spiral staircase: the angular slope of each band $\mathrm{d}\zeta/\mathrm{d}\psi$ is independent of ρ, whereas the local, Cartesian slope must vary with ρ^{-1}. This idealization is the basis for our linearized stability analysis in Part 1 and predicts trends of angular amplitude in figure 11 that parallel the dashed curves. What we actually see in the figure is a radial variation between these two end members: the overall trend of amplitude with radius has a roughly constant angle θ, consistent with stability-analysis results for peak growth rate as a function of the local band angle (Takei & Katz 2013). However, the overall trend is composed of subtrends that follow spiral-staircase trajectories. This hybridization is a consequence of spiral-staircase bands that branch and merge with radius, to maintain an orientation close to the local angle for optimal growth. The azimuthal sections in figure 9 support this interpretation.

Although the broad trends in figure 11 are similar for $R = 0.1$ and $R = 1$, there are notable differences between figure 11(*a*) and (*b*). The effect of base-state segregation that was evident in figure 10 is also evident here: in figure 10(*a*), amplitude is concentrated at distal radii, whereas figure 10(*b*) displays significant amplitude at proximal radii. The proximal increase of spectral amplitude in figure 10(*b*) is broadly distributed in angle θ, indicating that the variations in porosity there are not in the form of coherently oriented bands, but are rather of blobby, isotropic form. Despite this incoherence at small ρ, spiral-staircase trajectories are still evident in figure 10(*b*), reflecting porosity-band structure at intermediate to distal radii. These results are surprisingly consistent with linearized stability analysis for $\tau = 0$, shown in figure 9(*f,i*) of Part 1.

3.2.4. *From fixed to dynamic anisotropy*

The preceding sections address the behaviour of the governing equations when the magnitude and direction of anisotropy are fixed. In all example calculations, we see the behaviour characteristic of shear with porosity-weakening viscosity: emergence of bands of higher porosity surrounded by compacted regions of lower porosity. The magnitude of anisotropy α controls the orientation of bands. For simulations with fixed anisotropy to reproduce the band orientation observed in simple-shear and torsion experiments requires saturated anisotropy, $\alpha \approx 2$.

Fixed-anisotropy results also demonstrate that gradients in shear stress can drive domain-scale liquid segregation, and that this base-state segregation affects the emergence and dynamics of porosity bands.

Fixed, uniform anisotropy may be a good approximation for simple shear at small strains when porosity, viscosity and strain-rate are nearly uniform throughout the domain. For Poiseuille and torsional flow, however, gradients in the driving stress are fundamental to the system configuration, and hence even a uniform-porosity initial state should contain variation in viscous anisotropy. For simplicity, this variation has been neglected above. To understand the effects of this simplification and to develop a more complete picture of the consequences of viscous anisotropy, we reintroduce dynamic anisotropy in the next section.

3.3. *Dynamic anisotropy*

The theoretical model of anisotropic viscosity presented in Part 1 specifies an instantaneous, equilibrium relationship between the viscous anisotropy tensor and the principal components of the stress tensor (based on Takei & Holtzman 2009*a*; Takei 2010). The magnitude of anisotropy α (shown in figure 4 of Part 1) is parameterized

as the hyperbolic tangent of the difference between principal stresses,

$$\alpha = 2\tanh\left[\frac{2(\sigma_3 - \sigma_1)}{\sigma_{sat}}\right]. \tag{3.1}$$

The direction of anisotropy Θ is defined by the angle between the shear plane and the direction of maximum tensile stress. This direction is restricted to be in the plane defined by the σ_1 and σ_3 axes for the unperturbed state at $\tau = 0$ (e.g. ζ–ψ for torsion), as was the case for static anisotropy. Here σ_1 and σ_3 are the minimum and maximum tensile stresses and σ_{sat} is a material parameter that must be specified. The dimensional value of the saturation stress is given by the product with background viscosity and shear-strain rate, $\eta_0\dot{\gamma}\sigma_{sat}$. For laboratory experiments (e.g. Holtzman *et al.* 2003), η_0 and $\dot{\gamma}$ are typically in the range 10^{10}–10^{11} Pa s and 10^{-4}–10^{-3} s^{-1}, respectively; $\sigma_{sat} \sim 1$ therefore corresponds to a stress of 1–100 MPa.

If $\sigma_3 - \sigma_1 \ll \sigma_{sat}$, the magnitude of anisotropy is effectively zero; for $\sigma_3 - \sigma_1 > \sigma_{sat}$, anisotropy saturates at $\alpha = 2$. Interesting choices are those where $2(\sigma_3 - \sigma_1)/\sigma_{sat} \lesssim 1$ because they allow for variation of α within the domain.

In simulations at their initial state, the principal components of the stress tensor are determined by the base-state flow. With time, however, porosity is redistributed by liquid segregation, modifying the viscosity structure and changing the distribution and orientation of stress. Indeed, as demonstrated by the results below, emergent variations in porosity are coupled to emergent variations in viscous anisotropy, with consequences for the overall behaviour of the system.

3.3.1. *Simple shear*

Figure 12 shows results from a simulation of simple shear with $R = 0.1$ and $\sigma_{sat} = 2$. In its initial state, the stress field is nearly uniform with $\sigma_3 - \sigma_1 = 1.17$ (there are small deviations due to the porosity perturbation). The associated initial anisotropy is also nearly uniform with $\alpha = 1.65$ and $\Theta = 45°$. A snapshot of porosity at strain $\gamma = 2.25$ is plotted in figure 12(*a*); it shows the typical pattern of low-angle porosity bands. Overlain on the porosity field are vectors representing the direction and magnitude of anisotropy. These fields have been subsampled to avoid obscuring the image with vectors. To leading order, the anisotropy is of uniform direction and magnitude; closer inspection reveals subtle variations that we quantify below.

Figure 12(*b*) shows the angular amplitude spectrum for the same simulation. It is strikingly similar to that shown in figure 4(*c*), which is derived from a simulation with fixed $\alpha = 2$. It bears little resemblance to figure 4(*b*) for fixed $\alpha = 1.5$, despite the fact that the average α in figure 12(*d*) is only 1.65 (see figure 2 for the predicted growth rate from linearized analysis at $\alpha = 1.65$). Furthermore, a careful comparison of figure 12(*b*) with figure 4(*c*) indicates that there is actually more amplitude at very low θ in the simulation with dynamic anisotropy, despite it having smaller average α. This suggests that nonlinear dynamics of variable-anisotropy flow promote the growth of porosity bands at angles lower than that predicted by linearized stability analysis.

Figure 12(*c*) supports this hypothesis by showing another difference between linearized stability analysis, fixed-anisotropy simulations and dynamic-anisotropy simulations. The heavy solid line shows the amplitude of the largest Fourier mode through progressive shear strain. Compare this line with the light solid line representing the prediction of linearized analysis, computed with α, Θ fixed at their spatiotemporal average from the simulation; unlike in figure 6, simulation and linearized analysis are a poor match. Furthermore, computing the predicted growth rate with values of α, Θ at their extremal values (dashed lines) still does not fit the

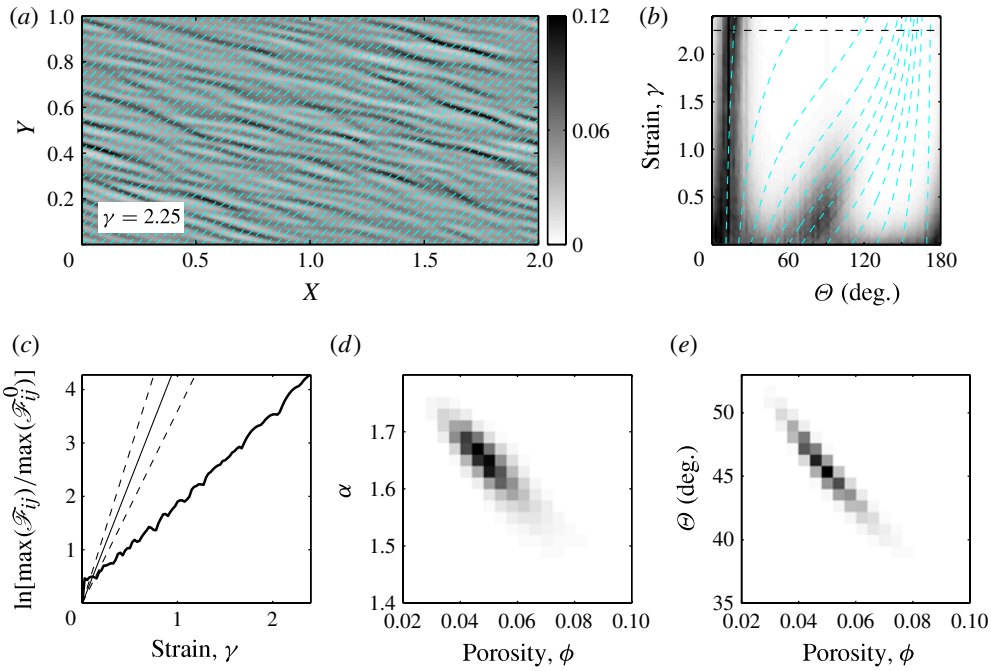

FIGURE 12. (Colour online) Results of a representative simulation of simple shear with dynamic anisotropy. For this model, $\sigma_{sat} = 2$ such that at $\tau = 0$, $\alpha = 1.650$ with a standard deviation 0.005 due to the porosity perturbation. Grid size is 1200×600. (*a*) The porosity distribution at a shear strain of 2.25. The (subsampled) anisotropy field is shown by vectors that are rotated by an angle Θ from the shear plane and scaled by α. (*b*) The angular amplitude spectrum as a function of strain γ with passive advection trajectories overlain. The horizontal dashed line marks the strain of the snapshot in (*a*). (*c*) Log-amplitude of the largest Fourier mode as a function of progressive strain, as in figure 6. The thick solid line is derived from the simulation; the thin solid line corresponds to peak growth predicted by linearized analysis with α, Θ taken as their spatiotemporal mean from the simulation. Dashed lines are based on linearized analysis with α, Θ equal to 1.5, 40° (high-porosity) and 1.7, 50° (low-porosity). (*d*) A two-dimensional histogram derived from the result shown in (*a*). The ranges of ϕ and α are divided into 20 adjacent bins; each grid cell in (*a*) is assigned to a bin according to its ϕ, α pair. Bins are blackened according to their number of entries. (*e*) A two-dimensional histogram as in (*c*), but for anisotropy angle, Θ.

simulation result. Again this points to the importance of nonlinearity under dynamic anisotropy.

An understanding of these counterintuitive results begins with a recognition of the correlations shown in figure 12(*d,e*). These plots are two-dimensional histograms derived from the grid cells of the simulation shown in figure 12(*a*). Paired values of α–ϕ (figure 12*d*) or Θ–ϕ (figure 12*e*) are sorted into a 20×20 array of equal-size bins; the bins are then associated with a greyscale value proportional to the number of entries. The histograms clearly show that high-porosity bands are associated with smaller, lower-angle anisotropy, while the compacted regions between bands are associated with larger, higher-angle anisotropy. Low viscosity in high-porosity regions lowers the magnitude of stresses there and correspondingly lowers the magnitude of anisotropy; at the same time, the same low viscosity promotes localization of shear onto the band, locally rotating the principal axes clockwise and reducing the angle of

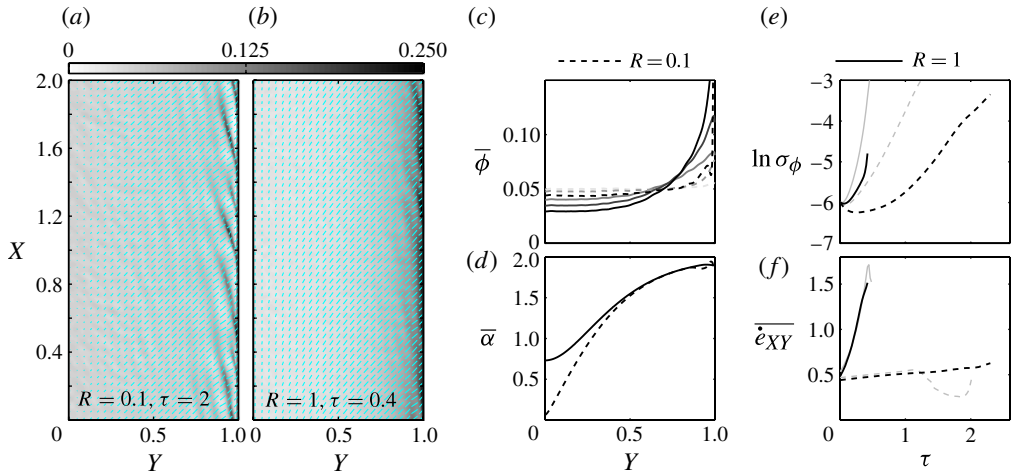

FIGURE 13. (Colour online) Results of two representative simulation of Poiseuille flow with dynamic anisotropy and $\sigma_{sat} = 2$. Grid size is 500×1000. (*a*), (*b*) The porosity distribution for $R = 0.1$ and $R = 1$, respectively. The (subsampled) anisotropy field is shown by vectors that are rotated by an angle Θ from the shear plane and scaled by α. (*c*) Profiles of the porosity, averaged in the X direction, as a function of Y, for both simulations. Darker lines are for later times τ; dashed lines ($R = 0.1$) at $\tau = 0.2$, 0.8, 2.0; solid lines ($R = 1$) at $\tau = 0.2$, 0.3, 0.4. (*d*) Profiles of the anisotropy magnitude, averaged in the X direction, as a function of Y, for both simulations ($\tau = 2$ for $R = 0.1$; $\tau = 0.4$ for $R = 1$). (*e*) The logarithm of the standard deviation of porosity at $Y = 0.9$ as a function of τ for both simulations (grey lines are for fixed-anisotropy simulations from figure 8). (*f*) The vertically averaged shear-strain rate at $Y = 0.9$ as a function of τ for both simulations (grey lines as in *e*).

anisotropy. There is a corresponding back-rotation of stresses in the compacted regions between bands, consistent with the vorticity perturbation shown in figure 5.

When a mature pattern of porosity bands exists, it is the compacted regions between bands that are most important for maintaining small θ: these regions are the site of emergent reconnections between existing bands, as discussed above in § 3.2.1. The compacted regions have larger α, which promotes relatively lower-angle bands, but the value of α is still less than 2, so this alone is not a sufficient explanation. What seems to be essential is the rotation of the σ_3 direction (and, hence, of Θ) to larger angles in the compacted regions. If the shear plane is locally back-rotated by an angle $\delta\Theta$, this same back-rotation should apply to porosity bands that emerge there; for such bands $\theta = \theta_{lsa} - \delta\Theta$, where θ_{lsa} is the band angle with peak growth rate predicted by linearized stability analysis. This interpretation is supported by figure 9 of Part 1, which shows that at larger fixed Θ, the low-angle growth-rate peak appears at lower angles. In simulations with dynamic anisotropy, however, Θ changes according to the local rotation of the principle axes, and so the rotation does not, in itself, reduce the amplitude of the low-angle peak, as it does for the stability analysis.

3.3.2. *Poiseuille flow*

As with fixed anisotropy, the results of simulations of Poiseuille flow with dynamic anisotropy reflect the simultaneous processes of base-state segregation, gravity-driven segregation and porosity-band formation. Figure 13 summarizes two simulations, both with $\sigma_{sat} = 2$. The snapshot in figure 13(*a*) has $R = 0.1$, while the snapshot in figure 13(*b*) has $R = 1$. Greyscale intensity in these figure is scaled to the porosity

field. Figure 13(*c*) shows vertically averaged porosity profiles as a function of Y, which document the extent of base-state segregation. Given the results in figure 7 above and in Part 1, we expect that base-state segregation will dominate in the case of $R = 1$; this is, in fact, supported by the results. Careful comparison with the porosity curve in figure 7(*f*) shows that base-state segregation is slightly enhanced by dynamic anisotropy.

Vectors in figure 13(*a,b*) map the variation in the magnitude and direction of anisotropy. Increasing shear stress in the Y direction causes an increase in α from low values at left to near-saturation at right, as shown by profiles of vertically averaged anisotropy magnitude in figure 13(*d*). The low values of α near $Y = 0$ are distinct from the fixed-anisotropy cases of figure 7(*c,f*), and this explains a difference in the base-state segregation: profiles of $\overline{\phi}$ from dynamic anisotropy simulations flatten near $Y = 0$, where α is small, in contrast with the profiles for fixed $\alpha = 2$ (figure 7).

Emergence of porosity bands near $Y = 1$ is also affected by dynamic anisotropy. Figure 13(*e*) shows that the increase in standard deviation of porosity that was observed for the case of fixed anisotropy is delayed and reduced under dynamic anisotropy. Combined with results for simple shear (§ 3.3.1), these plots suggest that band emergence is delayed by the small fluctuations of anisotropy at the scale of the bands. Band-scale fluctuations in anisotropy do not affect base-state segregation, however, and so the balance of the two modes shifts toward base-state segregation. This change in mode balance could explain the slight enhancement of base-state segregation, in spite of smaller α; the diminished growth of low-angle channels is favourable for base-state segregation. Even under dynamic anisotropy, high-porosity bands do eventually form as a consequence of the increasing rate of shear strain associated with base-state segregation. Inspection of figure 13(*a*) suggests that the angle between porosity bands and the shear plane is lower under dynamic anisotropy than under fixed anisotropy, as was the case for simple shear.

3.3.3. *Torsional flow*

Figure 14 presents two representative results for torsional flow with dynamic anisotropy ($\sigma_{sat} = 2$). Figures 14(*a,b*) plot porosity on slices through the three-dimensional domain of simulations with $R = 0.1$ and $R = 1$, respectively. A comparison of these results with figure 9 highlights a striking difference: porosity-band amplitude is significantly reduced relative to the case of fixed anisotropy. This is consistent with the analysis of simple shear with dynamic anisotropy (§ 3.3.1), which showed that the rate of band growth is diminished. It is also consistent with the analysis of dynamic-anisotropy Poiseuille flow (§ 3.3.2), which showed a relative enhancement of base-state segregation over band emergence. Figure 10(*c*) is a plot of the mean and standard deviation of porosity as a function of radius. The mean porosity (black), in comparison with fixed anisotropy (figure 10), shows that the base-state segregation is reduced by dynamic anisotropy; this may be explained by the smaller value of α and the diminished growth of high-permeability channels. The standard deviation curves (grey, shown in magenta online) show that porosity variations are muted throughout the domain. Even for $R = 0.1$, which showed strong banding at distal radii under $\alpha = 2$, porosity variations are concentrated at proximal radii. This reflects the diminished growth rate of bands relative to base-state segregation under dynamic anisotropy, even at distal radii.

These differences from fixed anisotropy can be understood by considering the variation of anisotropy magnitude α throughout the domain. Figure 14(*d*) shows the mean and standard deviation of α as a function of radius. Here $\overline{\alpha}$ increases with ρ

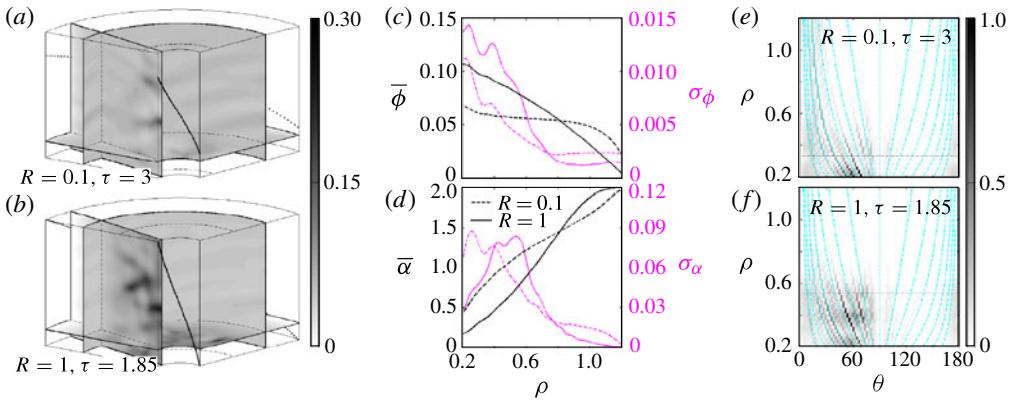

FIGURE 14. (Colour online) Results of two representative simulations of torsional flow with dynamic anisotropy and $\sigma_{sat} = 2$. Grid size is $150 \times 150 \times 150$. (*a*), (*b*) The porosity distribution for $R = 0.1$, $\tau = 3$ and $R = 1$, $\tau = 1.85$, respectively. Black lines are as in figure 9. (*c*) The mean (black) and standard deviation (grey, shown in magenta online) of porosity, taken over the ψ and ζ directions, as a function of radius ρ. (*d*) The mean (black) and standard deviation (grey, shown in magenta online) of anisotropy magnitude as a function of ρ. (*e*), (*f*) Angular amplitude spectra as a function of radius ρ, computed from the porosity fields shown in (*a*) and (*b*), respectively. Horizontal dashed lines mark the radius at which the cylindrical shear strain in a ψ–ζ plane is unity.

due to the increasing strain rate imposed by the boundary conditions. Smaller values of α at proximal radii reduce the base-state decompaction there, relative to fixed $\alpha = 2$. Despite this, the variation of anisotropy, captured by σ_α (grey lines, shown in magenta online, in figure 14*d*) and σ_Θ (not shown) is largest at proximal radii.

Figure 14(*e*,*f*) show the angular amplitude spectra as a function of radius, and can be compared with figure 11. The spectra show two distinct distributions of amplitude. At distal radii, amplitude is concentrated at small angle, whereas at proximal radii, amplitude is spread more broadly up to a limit of $\theta = 90°$. The transition between these two regimes takes place at radii where $1 < \alpha < 1.5$; this is consistent with the growth-rate curves computed by stability analysis for different values of α in figure 9(*d*) of Part 1. It is interesting to note that despite this dichotomy, there are peaks in the spectra that follow spiral-staircase trajectories, suggesting that some features of the porosity field span a broad set of radii.

3.3.4. *Summary of dynamic anisotropy*

Under our reformulation of the theory by Takei & Holtzman (2009*a*), anisotropy is characterized by a magnitude α and an angle Θ; these are set according to the principal stresses and the constant, non-dimensional, reference stress, σ_{sat}. Results presented above are obtained with $\sigma_{sat} = 2$ because it leads to significant variation of α within the domain; much larger or much smaller values of σ_{sat} would effectively result in fixed α (zero or saturated). A saturated dynamic anisotropy would, however, still allow for variation in Θ, which is an interesting case for future consideration.

Simple-shear simulations, with their uniform base-state stress and strain rate, demonstrated that α and Θ vary systematically with porosity. They showed that the growth rate of porosity bands is diminished by dynamic anisotropy, even if the variations of α and Θ are small. They also indicate that simple shear under variable

anisotropy yields reduced band angles relative to that under fixed anisotropy with $\alpha = 2$; this despite the fact that under dynamic anisotropy $\overline{\alpha} < 2$.

The subtleties introduced by dynamic anisotropy in simple shear also apply to Poiseuille and torsional flow. In those cases, however, there is the further complication of a non-uniform base state, which is reflected and modified by spatial variation in α. For Poiseuille flow, base-state segregation is enhanced by dynamic anisotropy, whereas for torsional flow it is diminished. In both cases, we see a relative reduction in the porosity variations associated with perturbation growth.

4. Discussion

Above we presented results of numerical simulations under three different flow regimes: simple shear, Poiseuille and torsion. We have applied different values of the non-dimensional compaction-length parameter R, and considered both fixed anisotropy and dynamic anisotropy. For fixed anisotropy, we considered different values of anisotropy magnitude, while holding the anisotropy direction fixed at 45° to the shear plane. In this section we discuss selected results in more detail, highlighting points where comparison may be made with experiments (although quantitative comparison with experiments is beyond the current scope).

In studying the results, it is important to consider the limitations of the model, both in terms of the assumptions used to derive the governing equations, and the approximations used to solve them. The underlying theory was proposed by Takei & Holtzman (2009*a*,*b*) to model a monomineralic aggregate of isotropic, solid grains surrounded by an interconnected network of liquid-filled pores. Of crucial importance is the assumption that the aggregate deforms by diffusion creep. Takei & Holtzman (2009*a*) used this assumption to derive a viscosity tensor that is applicable under an arbitrarily evolving orientation of the principal components of stress. In Part 1 we propose a simplified viscosity tensor, based on the assumption that the maximum and minimum principal stresses are confined to the surface on which they reside under the base-state flow. For simple shear and Poiseuille, this surface is flat and coincides with the domain; for torsional flow the surface is cylindrical and parallel to the ζ axis. If this assumption were removed, emergent heterogeneity of stress would likely cause out-of-plane deviations of the σ_1 and σ_3 directions; our results from § 3.3 suggest that even if these deviations are small, their results could be significant. We leave this question for future work.

In the present study we applied a finite-volume discretization to the governing partial differential equations, converting them into a system of coupled, nonlinear, algebraic equations. Benchmark calculations in § 3.1 showed that solutions to this discrete system are convergent for small porosity (where the governing equations are valid). Our benchmark also revealed the minimum resolution needed to accurately model perturbation growth, and showed that insufficient resolution results in the artificial suppression of porosity bands. These results are especially important when considering flows where two modes of segregation occur simultaneously. The resolution required to accurately model porosity bands is significantly greater than that needed to capture base-state segregation. This becomes a problem for three-dimensional simulations where computational cost limits the available resolution. So while our results for simple shear and Poiseuille are probably unbiased by discretization, there is no doubt that under torsion, porosity-band emergence should be more rapid and at smaller wavelengths than predicted here.

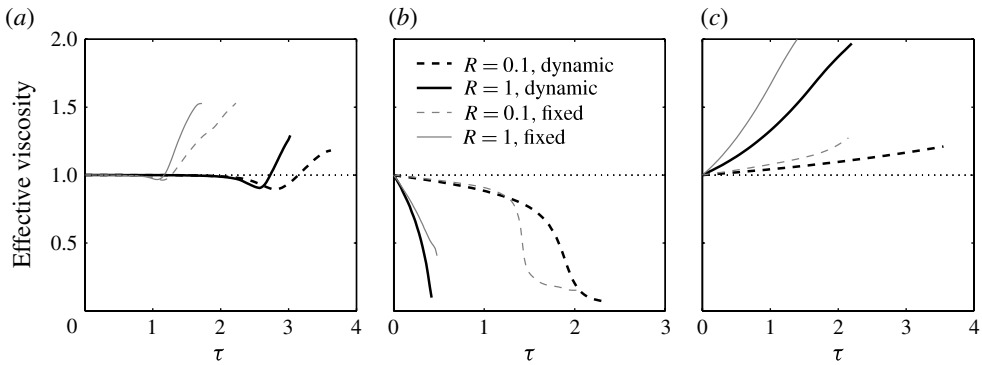

FIGURE 15. Effective viscosity as a function of non-dimensional time in simple shear (*a*), Poiseuille (*b*) and torsional flow (*c*). Black lines represent dynamic anisotropy, grey lines represent fixed $\alpha = 2$. Dashed and solid lines correspond to $R = 0.1$ and $R = 1$, respectively.

We showed in § 3.2.2 that the growth-rate of porosity bands is also sensitive to the amplitude of the initial porosity perturbation. The characteristics of this perturbation in laboratory experiments on partially molten aggregates is poorly constrained, but thought to be around 20 % of ϕ_0 (D. Kohlstedt, Personal communication, 2012). The wavelength spectrum of the perturbation in experiments is also unknown. In the simulations presented above, we have assumed a flat spectrum that is set to zero at wavelengths smaller than 15 times the grid spacing, because at smaller wavelengths, numerical diffusion artificially damps growth. Simple shear simulations conducted with larger cut-off wavelength (and, hence, smoother perturbation fields) lead to broader, more widely spaced porosity bands. We raise this point to highlight the importance of the initial perturbation's detailed structure, but we defer further consideration to future work.

Bearing the above caveats in mind, results from both this paper and Part 1 show that anisotropic viscosity is a plausible alternative to the hypothesis of Katz *et al.* (2006), who stated that the low angle of porosity bands to the shear plane in experiments is a consequence of non-Newtonian viscosity.

Laboratory experiments on torsional and Poiseuille flow provide an opportunity to test predictions of the anisotropic-viscosity hypothesis. In particular, it should be possible to assess the existence of a base-state mode of segregation driven by gradients in stress or strain rate. Based on present work, we expect that torsional flow experiments will cause migration of liquid toward the centre of the experiment, with an emergent gradient in porosity from distal to proximal radii. Poiseuille flow experiments should exhibit base-state segregation of liquid toward the no-slip walls (in parallel plate or, more accessibly, in pipe geometry).

Laboratory experiments typically monitor both the driving force causing deformation and the displacement rate of the boundary where the force is applied. This relationship between applied force and consequent flow can be used to define an effective viscosity: the bulk resistance to deformation (e.g. Holtzman *et al.* 2005). Liquid segregation and redistribution through the sample can cause this viscosity to evolve over progressive strain.

Simulations demonstrate the link between liquid segregation and effective viscosity. Figure 15 shows the evolution of effective viscosity from simulations on simple shear, Poiseuille and torsional flow, for two values of the dimensionless compaction length

and for both fixed ($\alpha = 2$) and dynamic ($\sigma_{sat} = 2$) anisotropy. In the case of simple shear, where the effective, non-dimensional shear-strain rate is imposed to be unity, the effective viscosity is computed as the mean shear stress, normalized to that at $\tau = 0$,

$$\eta_{eff}(\tau) = \overline{\sigma_{XY}}(\tau)/\overline{\sigma_{XY}}(\tau = 0), \tag{4.1}$$

where the mean is taken over a subregion of the domain that includes all X and $1/3 \leqslant Y \leqslant 2/3$. Figure 15(*a*) shows that during the formation of porosity bands, the effective viscosity of the sample remains approximately constant. It is only when liquid segregation creates porosity near unity in bands and near zero between them that the effective viscosity deviates substantially from its initial value. In contrast, the effective viscosity of Poiseuille flow decreases continuously from $\tau = 0$ due to segregation of melt up the stress gradient. Because the shear stress increases linearly across the sample toward the no-slip boundary condition imposed at $Y = 1$, the effective viscosity is proportional to the inverse of the mean, vertical flow speed of the solid at $Y = 0$,

$$\eta_{eff}(\tau) = \left[\overline{\boldsymbol{V}}(Y = \tau = 0) \cdot \hat{\boldsymbol{e}}_X\right] / \left[\overline{\boldsymbol{V}}(Y = 0, \tau) \cdot \hat{\boldsymbol{e}}_X\right]. \tag{4.2}$$

As liquid concentrates in the zone of larger shear stresses at $Y = 1$, it reduces the viscosity there, focusing shear strain and increasing the speed of the gravity-driven, downward flow of the aggregate. The diminished resistance to flow is plotted in figure 15(*b*). Since larger compaction length causes faster base-state segregation, it also causes a more rapid decrease in effective viscosity. The effect of compaction length is also evident in figure 15(*c*), for torsional flow, but the trend of effective viscosity there is increasing, rather than decreasing. The effective viscosity for torsional flow is computed as

$$\eta_{eff}(\tau) = \overline{\rho^2\sigma_{\psi\zeta}}(\tau)/\overline{\rho^2\sigma_{\psi\zeta}}(\tau = 0), \tag{4.3}$$

where averages are taken over all ρ, all ψ, and $1/3 \leqslant \zeta \leqslant 2/3$. The effective viscosity of torsional flow increases continuously from $\tau = 0$ due to base-state segregation, which drives liquid inward. This increases the viscosity at distal radii where higher stress is supported, while decreasing the viscosity at proximal radii where the stress is lower. The net result is an increasing effective viscosity. As the effective viscosity increases, a greater torque is needed to maintain the constant twist rate. The difference between fixed- and dynamic-anisotropy curves under torsion may arise because porosity bands provide a fast pathway for base-state segregation.

Simulations therefore predict that base-state segregation controls the effective viscosity. There is no evidence in the curves plotted in figure 15 that emergence of a banded porosity structure directly influences it (except in figure 15(*a*) at late times, when porosity bands develop into what is more accurately described as liquid-filled pockets). This is in contrast with reports by experimentalists (Holtzman *et al.* 2005; King, Holtzman & Kohlstedt 2011), which suggest that high-porosity bands reduce the effective viscosity. Bands that span the entire sample in an alignment subparallel to the shear plane would strongly localize deformation, and hence would accommodate most of the shear displacement onto a low-viscosity region. In experiments, however, porosity bands do not take this form and are not observed to accommodate the majority of shear strain. Instead, observations suggest partial localization such that strain remains distributed between low- and high-porosity regions (Holtzman *et al.* 2003; King *et al.* 2010). Understanding the discrepancy between effective viscosity as predicted here and as measured in experiments may reveal information about the rheology of partially molten aggregates.

Published experiments on partially molten, synthetic rocks deformed in torsion may, in fact, constitute evidence for base-state segregation. King *et al.* (2011) constructed composite cylinders for torsion experiments by wrapping an inner cylinder of one aggregate in an outer ring of a different aggregate. The basaltic-melt-bearing aggregate was termed the source, and the melt-free aggregate was termed the sink. In one set of experiments, the source aggregate constituted the outer ring and the sink aggregate was used for the inner cylinder. In the second set of experiments, this arrangement was reversed. King *et al.* (2011) then investigated the radial segregation of melt under torsional flow. In the first set of experiments with the outer-ring source, melt transport penetrated deeply inward, into the sink region; it penetrated well beyond the porosity-banded region at distal radii. The second set of experiments, with an inner-cylinder source, produced only a small outward penetration of melt flow into the sink region. This latter flow was substantially less than in the first experiment, and seemed confined to occur along the extension of porosity bands.

King *et al.* (2011) cite surface tension and porosity-band formation as the forces driving radial flow. They explain the difference between the two configurations as arising from delayed band formation in the case of an inner-cylinder source. In the present set of papers we have shown the porosity-band mode of liquid segregation occurs normal to the shear plane, not parallel to it. We therefore dispute the hypothesis that pressure gradients associated with band formation drive radial melt segregation. Instead, the experimental results from King *et al.* (2011) are readily interpreted in terms of cooperation and competition of surface tension and base-state melt segregation. Base-state segregation drives the melt inward, toward the centre of the cylinder, whereas surface tension drives melt toward the sink region. If the melt starts in an outer-ring source, both of these forces drive melt inward, consistent with the observed strong penetration. On the other hand, if the melt starts in an inner cylinder, the two forces work in opposite directions; this competition is consistent with the observed weak penetration. Hence, it seems possible that the experimental results of King *et al.* (2011) provide evidence for base-state flow.

If this is the case, it predicts that experiments will develop a negative radial porosity gradient in the source region. This prediction should be checked against experiments. If the compaction length in experiments is small, present theory predicts that the porosity gradient should be muted in amplitude.

Earlier torsional deformation experiments by King *et al.* (2010) are simpler than those described above; they are performed on a single aggregate of olivine grains and basaltic melt. These experiments produce robust patterns of low-angle porosity bands, especially at distal radii. Base-state segregation may be present in experiments by King *et al.* (2010), but it is not dominant. This balance between modes of segregation can be understood in the context of present theory if the compaction length is much smaller than the experimental sample. The compaction length estimated by King *et al.* (2010) is ~ 0.5 mm in a sample of ~ 5 mm in height, giving $R \approx 0.1$. However, the strongly banded porosity structure in experiments is more consistent with the *fixed* anisotropy simulation in figure 9(*a*); whereas the absence of obvious base-state segregation is more consistent with the dynamic anisotropy calculation in figure 14(*a*). This discrepancy may indicate an issue in the details of the model for the magnitude of viscous anisotropy in (3.1), or a more fundamental problem. For example, model behaviour may vary if anisotropy is out of equilibrium with the principal stresses, contrary to what we have assumed. Either way, future work must investigate the details of dynamic anisotropy.

5. Conclusion

The present work builds on the results of Part 1 to understand the consequences of anisotropic viscosity in a deforming, two-phase aggregate. The linearized stability analysis presented there and the numerical simulations presented here reach the same conclusions where they have an overlapping focus (i.e. at small times τ, when nonlinear interactions are negligible and the perturbations to the porosity field remain small). The numerical simulations extend the scope of our analysis, however, and the conclusions that we reach by this extension are summarized below.

(i) Simulations of simple shear with fixed, saturated anisotropy produce low-angle bands. The bands are maintained at low angle up to moderate strains by two processes: reconnection of bands and back-rotation of the compacted regions between bands.

(ii) Simulations of parallel-plate Poiseuille flow with fixed, saturated anisotropy exhibit three modes of liquid segregation that interact over finite time: gravity-driven, base-state and porosity-band segregation. Base-state flow causes shear-strain localization near the no-slip wall, which increases the growth rate of porosity bands there. Even for compaction lengths at the scale of the domain or larger, when the base-state flow is initially dominant, bands emerge as a consequence of this interaction. The bands, in turn, change the permeability structure and affect gravity-driven and base-state segregation.

(iii) Simulations of torsional flow with fixed, saturated anisotropy exhibit a competition between base-state and porosity-band segregation. At smaller compaction length where the latter is dominant, the high-permeability bands enhance radial segregation. The spiral-staircase pattern of porosity bands is modified by reconnections at intermediate to proximal radii that keep band-angles low. At larger compaction length, when base-state segregation is dominant, liquid is removed from the distal radii where bands would form.

(iv) Dynamic anisotropy modifies simulations of simple shear by reducing the rate of porosity-band growth, and reducing the dominant angle of bands to the shear plane. Reconnections and back-rotation are still active. Some reconnections emerge with an orientation parallel to the nominal shear plane.

(v) Under Poiseuille and torsional flow, dynamic anisotropy also lowers the angle between porosity bands and the shear plane. Moreover, at any given compaction length, it favours base-state segregation by lowering the rate of band growth. Simulations of torsional flow, however, were performed at a resolution that artificially suppresses porosity-band emergence and hence they may not accurately model the balance between the two modes of segregation.

(vi) The evolution of effective viscosity in simulations is associated with base-state segregation. In simple shear, which has no base-state segregation, effective viscosity is approximately constant until porosity bands reach porosities near unity (which does not occur in experiments). Under Poiseuille flow, base-state segregation concentrates liquid towards higher stress, reducing the effective viscosity and hence increasing the downward flux of the two-phase system. Under torsional flow, base-state segregation moves liquid toward lower stress, increasing the effective viscosity and hence increasing the torque required to maintain the constant twist rate.

(vii) Although unrecognized previously, base-state segregation may actually play an important role in published torsion experiments that investigate radial melt

transport (King *et al.* 2011). Other experiments by King *et al.* (2010) suggest that the compaction length in these experiments is small, and hence base-state flow is weak relative to band formation. Predictions of base-state segregation by simulations and stability analysis in this two-paper set are testable if experimentalists take careful measurements of radial porosity profiles in torsional and/or Poiseuille flow configurations.

Acknowledgements

The authors acknowledge stimulating discussions with D. L. Kohlstedt and C. Qi, and thank M. Spiegelman, G. Simpson, S. Butler and an anonymous reviewer for their helpful suggestions. Simulations were run on the UK national supercomputer (HECToR) and clusters provided by the Oxford Supercomputing Centre. Y.T. visited the University of Oxford in 2011 with support of the Royal Society; R.F.K. visited the Earthquake Research Institute at the University of Tokyo in 2012 with support from the International Research Office.

REFERENCES

AMESTOY, P. R., DUFF, I. S., L'EXCELLENT, J. Y. & KOSTER, J. 2001 A fully asynchronous multifrontal solver using distributed dynamic scheduling. *SIAM J. Matrix Anal. Appl.* **23** (1), 15–41.

BALAY, S., BUSCHELMAN, K., GROPP, W. D., KAUSHIK, D., KNEPLEY, M., MCINNES, L. C., SMITH, B. F. & ZHANG, H. 2001 Portable, Extensible Toolkit for Scientific Computation, http://www.mcs.anl.gov/petsc.

BALAY, S., BUSCHELMAN, K., GROPP, W. D., KAUSHIK, D., KNEPLEY, M., MCINNES, L. C., SMITH, B. F. & ZHANG, H. 2004 PETSc Users Manual. *Tech. Rep.* Argonne National Lab.

BUTLER, S. L. 2009 The effects of buoyancy on shear-induced melt bands in a compacting porous medium. *Phys. Earth Planet. Inter.* **173** (1–2), 51–59.

BUTLER, S. L. 2012 Numerical models of shear-induced melt band formation with anisotropic matrix viscosity. *Phys. Earth Planet. Inter.* **200–201**, 28–36.

CAI, X.-C., KEYES, D. E. & VENKATAKRISHNAN, V. 1997 Newton–Krylov–Schwarz: an implicit solver for CFD. In *Proceedings of the Eighth International Conference on Domain Decomposition Methods*, pp. 387–400.

HOLTZMAN, B. K., GROEBNER, N. J., ZIMMERMAN, M. E., GINSBERG, S. B. & KOHLSTEDT, D. L. 2003 Stress-driven melt segregation in partially molten rocks. *Geochem. Geophys. Geosyst.* **4**, 1227–1230.

HOLTZMAN, B. K., KOHLSTEDT, D. L. & MORGAN, J. PHIPPS 2005 Viscous energy dissipation and strain partitioning in partially molten rocks. *J. Petrol.* **46** (12), 2569–2592.

KATZ, R. F., KNEPLEY, M. G., SMITH, B., SPIEGELMAN, M. & COON, E. T. 2007 Numerical simulation of geodynamic processes with the Portable Extensible Toolkit for Scientific Computation. *Phys. Earth Planet. Inter.* **163**, 52–68.

KATZ, R. F., SPIEGELMAN, M. & HOLTZMAN, B. 2006 The dynamics of melt and shear localization in partially molten aggregates. *Nature* **442**, 676–679.

KING, D. S. H., ZIMMERMAN, M. E. & KOHLSTEDT, D. L. 2010 Stress-driven melt segregation in partially molten olivine-rich rocks deformed in torsion. *J. Petrol.* **51**, 21–42.

KING, D. S. H, HOLTZMAN, B. K. & KOHLSTEDT, D. L. 2011 An experimental investigation of the interactions between reaction-driven and stress-driven melt segregation: 1. Application to mantle melt extraction. *Geochem. Geophys. Geosyst.* **12**.

KOHLSTEDT, D. L & HOLTZMAN, B. K 2009 *Shearing Melt Out of the Earth: An Experimentalist's Perspective on the Influence of Deformation on Melt Extraction* **37**, 561–593.

MCKENZIE, D. 1984 The generation and compaction of partially molten rock. *J. Petrol.* **25**, 713–765.

SPIEGELMAN, M. 2003 Linear analysis of melt band formation by simple shear. *Geochem. Geophys. Geosyst.* **4** (9), 8615.

STEVENSON, D. J. 1989 Spontaneous small-scale melt segregation in partial melts undergoing deformation. *Geophys. Res. Lett.* **16**, 1067–1070.

TAKEI, Y. 2010 Stress-induced anisotropy of partially molten rock analogue deformed under quasi-static loading test. *J. Geophys. Res.* **115**, B03204.

TAKEI, Y. & HOLTZMAN, B. K. 2009*a* Viscous constitutive relations of solid–liquid composites in terms of grain boundary contiguity: 1. Grain boundary diffusion control model. *J. Geophys. Res.* **114**, B06205.

TAKEI, Y. & HOLTZMAN, B. K. 2009*b* Viscous constitutive relations of solid–liquid composites in terms of grain boundary contiguity: 2. Compositional model for small melt fractions. *J. Geophys. Res.* **114**, B06206.

TAKEI, Y. & HOLTZMAN, B. K. 2009*c* Viscous constitutive relations of solid–liquid composites in terms of grain boundary contiguity: 3. causes and consequences of viscous anisotropy. *J. Geophys. Res.* **114**, B06207.

TAKEI, Y. & KATZ, R. F 2013 Consequences of viscous anisotropy in a deforming, two-phase aggregate. Part 1. Governing equations and linearized analysis. *J. Fluid Mech.* **734**, 424–455.

TROMPERT, R. A. & HANSEN, U. 1996 The application of a finite volume multigrid method to three-dimensional flow problems in a highly viscous fluid with variable viscosity. *Geophys. Astrophys. Fluid Dyn.* **83**, 261–291.

ZIMMERMAN, M. E., ZHANG, S. Q., KOHLSTEDT, D. L. & KARATO, S. 1999 Melt distribution in mantle rocks deformed in shear. *Geophys. Res. Lett.* **26** (10), 1505–1508.